https://doi.org/10.5194/egusphere-2026-1681
Preprint. Discussion started: 27 April 2026

Global aerosol composition constraints from simultaneous data assimilation of satellite AOD and trace gas observations

Takashi Sekiya[1], Kazuyuki Miyazaki[2], Henk Eskes[3], Pieter Rijsdijk[3,4,5], Kengo Sudo[6], and Yugo Kanaya[1]

[1]Japan Agency for Marine-Earth Science and Technology, Yokohama, Japan
[2]Jet Propulsion Laboratory/California Institute for Technology, Pasadena, CA, USA
[3]Royal Netherlands Meteorological Institute (KNMI), De Bilt, the Netherlands
[4]Space Research Organisation Netherlands (SRON), Leiden, Netherlands
[5]Department of Earth Sciences, Vrije Universiteit, Amsterdam, the Netherlands
[6]Graduate School of Environmental Studies, Nagoya University, Nagoya, Japan

Correspondence: Takashi Sekiya (tsekiya@jamstec.go.jp)

Abstract.

The integration of satellite aerosol optical depth (AOD) and trace gas observations using data assimilation has the potential to improve our understanding of aerosol composition. This study evaluates these synergistic effects through combined constraints on total aerosols by AOD and on secondary aerosol formation by trace gases. The simultaneous data assimilation (DA) of NO_2, SO_2, CO, and HNO_3 from OMI, TROPOMI, MOPITT, and MLS, together with AOD from MODIS and VIIRS, improved aerosol analyses in most cases compared to conventional DA runs that separately assimilate AOD or trace gases satellite observations. Validation against independent surface observations of sulfate, nitrate, and ammonium (SNA), and $PM_{2.5}$ showed improved agreements by 6–98% compared to the conventional DA runs and the control simulation without any data assimilation. Notably, the reduction in $PM_{2.5}$ model biases exceeded that achieved by the conventional DA of AOD by 56% in Northeast Asia. These improvements were achieved by reduced SO_2 and soil dust emissions by 30% and 60% globally and increased NO_x and carbonaceous aerosol emissions by 30% and 15%. The simultaneous DA provides even larger reductions in SNA and AOD biases by up to 25% and 48% respectively, when the current generation instruments (TROPOMI and VIIRS) is used, instead of the previous generation instruments (OMI and MODIS). This coupled aerosol and trace gas DA framework offers significant advantages for improving global aerosol composition analyses, informing policy decisions with co-benefits for air quality and climate, and optimizing the use of the current satellite observing network.

1 Introduction

Exposure to high concentrations of fine particulate matter smaller than 2.5 μm in diameter ($PM_{2.5}$) adversely affects human health, causing respiratory and cardiovascular diseases, lung cancer, and premature mortality (Chen and Hoek, 2020). The global annual premature mortality caused by exposure to ambient $PM_{2.5}$, in the present day (2015–2019), is estimated to be approximately 4–9 million (Cohen et al., 2017; Burnett et al., 2018). Current risks of ambient particulate matter in 2019 have increased by 67.7% compared to those in 1990 (Murray et al., 2020). Aerosols also affect the Earth's radiative budget by

https://doi.org/10.5194/egusphere-2026-1681
Preprint. Discussion started: 27 April 2026

scattering and absorbing solar radiation. The radiative forcing relative to the pre-industrial era was estimated to be approximately 1.1 W m^{-2} (Smith et al., 2020) and partially masked the warming caused by greenhouse gases (IPCC, 2021). As the characteristics of an aerosol's microphysical structure (i.e., shape and size) and chemical composition determine its impacts on human health (Xue et al., 2021) and climate (Li et al., 2022a), detailed information on aerosol composition on a global scale is required for accurate impact assessments.

Satellite instruments have observed global distributions of aerosol optical depth (AOD) and vertical profiles of extinction coefficient for more than 20 years (Remer et al., 2024), including Advanced Very High Resolution Radiometer (AVHRR) (Hsu et al., 2017), Moderate Resolution Imaging Spectroradiometer (MODIS) (Sayer et al., 2013; Remer et al., 2020), Multi-angle Imaging SpectroRadiometer (MISR) (Garay et al., 2020), and Visible Infrared Imaging Radiometer Suite (VIIRS) (Lee et al., 2024). Furthermore, Polarization and Directionality of the Earth's Reflectances (POLDER) (Fu et al., 2020) and Cloud-Aerosol Lidar with Orthogonal Polarization (CALIOP) (Winker et al., 2013) provides more detailed information on aerosol size and vertical distributions, respectively. Long-term records of satellite AOD observations, such as MODIS and VIIRS, provide constraints on spatial and temporal variations in aerosols through direct modification of total aerosol concentrations with data assimilation technique (e.g., Randles et al., 2017; Yumimoto et al., 2017; Garrigues et al., 2022). For example, MERRA-2 aerosol reanalysis data (Randles et al., 2017) were produced by integrating satellite (AVHRR, MODIS, and MISR AOD) and ground-based remote sensing observations (AERONET AOD). These measurements have been applied for top-down estimation of aerosols and their precursor emissions (e.g., Huneeus et al., 2013; Yumimoto and Takemura, 2015; Jin et al., 2022; Tsikerdekis et al., 2023). Tsikerdekis et al. (2023) estimated dust, OA, BC, and SO_2 emissions using AOD, Ångström exponent, and single-scattering albedo derived from POLDER-3/PARASOL. However, analyses of aerosol chemical composition generally rely on forecast model information, as most AOD observations lack explicit information on aerosol composition.

Aerosol precursor gases represent another important source of information for constraining aerosol composition. Satellite observations of aerosol precursor gases, such as NO_2 (Boersma et al., 2018; van Geffen et al., 2022), SO_2 (Li et al., 2013; Theys et al., 2021), NH_3 (Van Damme et al., 2014; Shephard and Cady-Pereira, 2015), HCHO (De Smedt et al., 2018), and C_5H_8 (Wells et al., 2022), have been widely used to derive top-down emission estimates through data assimilation and inversion techniques (e.g., Miyazaki et al., 2021; van der A et al., 2024; Qu et al., 2022; Cao et al., 2022; Ding et al., 2024; Oomen et al., 2024). Our system with aerosol precursor emission analysis was uniquely able to capture spatial and temporal variations in secondary inorganic aerosols during the COVID-19 lockdown (Sekiya et al., 2023).

Satellite observations of aerosols and their precursors have not been jointly integrated into data assimilation applications in a fully coupled way that simultaneously optimize concentrations and emissions of aerosols and their precursor gases. Such integration is expected to provide improved constraints on individual aerosol components. In this study, we integrated satellite observations of AOD and trace gases using a state-of-the-art data assimilation technique, and evaluated their relative importance for constraining $PM_{2.5}$ and its composition. Furthermore, we assessed the impact of assimilating the current generation satellite constellation consisting of Sentinel-5P/TROPOMI and Suomi-NPP + NOAA-20/VIIRS, and compared the results to an

https://doi.org/10.5194/egusphere-2026-1681
Preprint. Discussion started: 27 April 2026

assimilation of observations from the previous generation constellation consisting of the Aura/OMI and Terra + Aqua/MODIS instruments.

The remainder of this paper is organized as follows: Section 2 describes the observational data for assimilation and validation, the data assimilation system, and the experiment setting used in this study. Sections 3 and 4 present the relative importance of AOD and trace gas observations on aerosol composition analyses and emission estimates, respectively. Section 5 assesses the impacts of assimilating the current and previous generation satellite constellations. Section **??** discusses remaining challenges and implications for health and climate impact assessments. Section 6 summarizes the study.

2 Data and Methods

2.1 Data assimilation system

2.1.1 Forecast model

We used the global chemical transport model CHASER V4.0 at a horizontal resolution of 1.1° with 32 vertical layers (Sudo et al., 2002; Sekiya et al., 2018), simulating tracer transport, emissions, dry and wet deposition, and chemical reactions (92 species and 262 reactions), including the ozone–HO_x–NO_x–CO–VOCs system and aerosol chemistry (sulfate–nitrate–ammonium, black carbon, organic carbon, dust, and sea salt). Aerosol thermodynamic equilibrium for the SO_4^{2-}-NO_3^--NH_4^+-Na^+-Cl^- system were considered with the ISORROPIA module (Nenes et al., 1998). The model includes heterogeneous chemical reaction of HNO_3 on the mineral dust surface using a simplified first-order irreversible uptake reaction with varying uptake coefficients from 1×10^{-5} to 1×10^{-3} as a function of relative humidity (e.g., Fairlie et al., 2010). The model represents soil dust and sea salt aerosols with 6 and 4 particle size bins (0.13, 0.33, 0.82, 1.27, 3.20, and 8.02 μm for dust and 0.178, 0.562, 1.78, and 5.62 μm for sea salt), respectively. The meteorological fields were simulated by the dynamical and physical modules of CHASER (i.e., the MIROC-AGCM model; (K-1 model developers, 2004)) with HadISST sea surface temperature and sea ice concentration (Rayner et al., 2003), and were nudged to the ERA5 meteorological reanalysis (Hersbach et al., 2020) with relaxation times of 5 days for air temperature and 0.7 days for horizontal winds.

The *a priori* NO_x, SO_2, CO, and carbonaceous aerosol emissions were obtained from the Community Emissions Data System (CEDS) v2021_04_21 inventory (Hoesly et al., 2018; O'Rourke et al., 2021) for anthropogenic sources, the Global Fire Emissions Database (GFED), version 4.1s inventory(Randerson et al., 2018) for biomass burning, and the Global Emissions Initiative (GEIA) soil NO_x inventory (Yienger and Levy II, 1995). The *a priori* soil dust emissions were derived from a dust emission scheme coupled with the model, which is a function of vegetation type, near-surface wind speed, soil moisture, and snow amount (Takemura et al., 2000).

The simulated AOD at a wavelength of 550 nm (τ) was calculated for comparison with satellite observations as follows:

$$\tau = \sum_{i=1}^{imax} \frac{\sigma_i q_i \Delta p}{g}, \quad (1)$$

https://doi.org/10.5194/egusphere-2026-1681
Preprint. Discussion started: 27 April 2026

where i indicates the aerosol species, σ_i is the mass extinction coefficient of the individual aerosol species, q_i represents the mass mixing ratio of the individual aerosol species, Δp stands for differences in air pressure between lower and upper bounds of individual model layers, and g is gravitational acceleration. For soil dust and sea salt, we used σ_i pre-calculated for 6 and 4 size bins, respectively (Takemura et al., 2002). For sulfate-nitrate-ammonium (SNA) and organic carbon (OC) aerosols, σ_i was treated as a function of relative humidity following Tang and Munkelwitz (1994) and Hobbs et al. (1997), respectively, considering hygroscopic growth of these aerosols. σ_i for SNA and anthropogenic OC aerosols were obtained by the standard Mie theory using number-weighted median radius, $R_{N,med}$ =0.11 μm and geometric standard deviation, $\sigma_g = 1.4$ derived from the KORUS-AQ observations (Titos et al., 2021), instead of standard settings (SNA: $R_{N,med}$ =0.058 μm, σ_g =1.6; OC: $R_{N,med}$ =0.1 μm, σ_g =1.6). σ_i for biomass-burning OC aerosols was calculated using $R_{N,med}$ =0.2 μm and σ_g =1.6 (Zhong et al., 2022).

2.1.2 Ensemble Kalman filter (EnKF) data assimilation

We used a state-of-the-art multi-constituent data assimilation system (Miyazaki et al., 2020a) based on the local ensemble transform Kalman filter (LETKF) technique (Hunt et al., 2007), as part of the Multi-model, multi-constituent chemical data assimilation (MOMO-Chem) framework (Miyazaki et al., 2020b). This system has been used for quantifying changes in atmospheric trace gases and their emissions (Miyazaki et al., 2017, 2021; Sekiya et al., 2023). In this study, we extended the data assimilation system to enable the simultaneous optimization of concentrations and emissions of aerosols and trace gases.

LETKF uses an ensemble forecast to estimate the background error covariance, under the assumption that the background ensemble perturbations adequately sample the model errors. The background ensemble model fields were converted into observation space using an observation operator, which included a spatial interpolation operator and an averaging kernel. The inclusion of averaging kernels in the observation operator accounts for vertically dependent sensitivities and eliminates the influence of the *a priori* profile shape (Eskes and Boersma, 2003).

The analysis ensemble mean $\bar{\boldsymbol{x}}^a$ was obtained by combining the background ensemble mean $\bar{\boldsymbol{x}}^f$ and assimilated observations y^o with relative weights determined by the background and observation error covariance matrices $\boldsymbol{X}^f$ and $\boldsymbol{R}$, respectively:

$$\bar{\boldsymbol{x}}^a = \bar{\boldsymbol{x}}^f + \boldsymbol{K}\left[\boldsymbol{y}^o - H(\bar{\boldsymbol{x}}^f)\right], \tag{2}$$

where $\boldsymbol{K}$ is the Kalman gain and H is the observation operator. The Kalman gain is given by:

$$\boldsymbol{K} = \boldsymbol{X}^f \tilde{\boldsymbol{P}}^a \left(\boldsymbol{H}\boldsymbol{X}^f\right)^T \boldsymbol{R}^{-1}, \tag{3}$$

where $\tilde{\boldsymbol{P}}^a$, which represents the analysis error covariance in the ensemble space, is given by:

$$\tilde{\boldsymbol{P}}^a = \left[\frac{(k-1)\boldsymbol{I}}{1+\Delta} + (\boldsymbol{H}\boldsymbol{X}^f)^T \boldsymbol{R}^{-1} (\boldsymbol{H}\boldsymbol{X}^f)\right]^{-1}, \tag{4}$$

where Δ is the multiplicative covariance inflation factor (=7% per data assimilation cycle) and k is the ensemble size (32 in this study).

https://doi.org/10.5194/egusphere-2026-1681
Preprint. Discussion started: 27 April 2026

For the AOD DA, we applied an observation error localization approach with a localization length (cut off length) of 500 km (1826 km), determined through sensitivity data assimilation calculations (Table S1). The self-consistency test of AOD DA with assimilated MODIS observations is summarized in Table S2. The parameter settings for the other observations followed those described in Miyazaki et al. (2020a).

Surface NO_x, CO, SO_2, carbonaceous aerosols (i.e., sum of BC+OM), and soil dust emissions were estimated based on a state argumentation method (e.g., Evensen, 2009), using the relationships between emissions and concentrations of related species in the background error covariance matrix generated by ensemble forecasts with perturbed emissions. We assumed that the size distribution of the emitted dust and the ratio of emitted black carbon to organic matter remained unchanged during the analysis step, because AOD retrievals at 550 nm alone does not constrain the size and composition of the primary aerosols. In the analysis step, the standard deviation of the emission ensembles was artificially inflated to a predefined minimum value, obtained from sensitivity calculations, to prevent covariance underestimation. The minimum values for NO_x, CO, SO_2, carbonaceous aerosol, and soil dust were set to 56%, 44%, 32%, 67%, and 48%, respectively. The minimum values for aerosol emissions were determined from the sensitivity calculations (Table S1).

Furthermore, we extend the state augmentation method to a simplified version of the two-stage bias estimation algorithm developed by Dee and Da Silva (1998) (see also Radakovich et al., 2001; Li et al., 2009) for emission estimates of carbonaceous aerosol and soil dust. The aerosol emission analyses and their biases were estimated as follows:

$$\bar{\boldsymbol{x}}^a = (\bar{\boldsymbol{x}}^f - \bar{\boldsymbol{b}}^f) + \boldsymbol{K}\left[\boldsymbol{y}^o - H(\boldsymbol{x}^f - \boldsymbol{b}^f)\right], \tag{5}$$

$$\bar{\boldsymbol{b}}^a = \bar{\boldsymbol{b}}^f - \alpha\boldsymbol{K}\left[y^o - H(\bar{\boldsymbol{x}}^f - \bar{\boldsymbol{b}}^f)\right], \tag{6}$$

where $\bar{\boldsymbol{b}}^a$ and $\bar{\boldsymbol{b}}^f$ indicate the analysis and first guess of the bias term, respectively. In practice, the bias forecast error covariance is unknown, and we therefore assume it to be $\alpha\boldsymbol{K}$ following Dee and Da Silva (1998). α was set to 0.5 (Li et al., 2009). We also assumed a persistence model for the bias forecast (i.e., the bias does not decay over time). The aerosol emission error covariance was artificially inflated using the additive inflation method (Mitchell and Houtekamer, 2000), by adding a small random noise with a normal distribution (mean = 0, standard deviation = 0.02). This approach substantially improved the estimation of dust emissions in the observing system simulation experiments, compared to the conventional augmentation methods (Table S3), because aerosol emissions are expected to have systematic (e.g., uncertainties in emission factors and dust parameterization) and random errors (e.g., timings of wildfires and dust strom events). However, this approach had no significant impacts on emissions of NO_x and SO_2 (not shown).

We applied the variable localization technique to eliminate error correlations between variables that may otherwise suffer from spurious correlations (Kang et al., 2011). Multiple-constituent observations could provide information on multiple species' emissions from individual sectors using error correlation between different variables, as suggested by Qu et al. (2022). However, this system prioritizes robustness in total emission estimates of individual species. We then reflect the emission estimates in secondary species, such as ozone, sulfate, and nitrate, during the forecast steps. Specifically, as summarized in Fig. 1, we used tropospheric NO_2 column observation for estimating NO_x emissions, total SO_2 column observations for SO_2 emissions, AOD with the observed Ångström exponent (α) of > 0.5 for primary carbonaceous aerosol emissions, and AOD

https://doi.org/10.5194/egusphere-2026-1681
Preprint. Discussion started: 27 April 2026

with α of ≤ 0.5 for soil dust aerosol emissions. AOD assimilation also optimized total aerosol mass concentrations during the analysis step. After the emission optimizations, during the forecast step, sulfate, nitrate, and ammonium mass concentrations, as well as many other species, were indirectly influenced by the updated NO_x and SO_2 emissions.

2.2 Observations for the assimilation

2.2.1 OMI and TROPOMI tropospheric NO_2 column

The OMI and TROPOMI instruments are ultraviolet/visible nadir-scanning solar-backscatter spectrometers (Levelt et al., 2006; Veefkind et al., 2012). Both instruments have a local equator crossing time of approximately 13:40 LT. The nadir ground pixel sizes of OMI and TROPOMI were 13×24 km^2 and 3.5×5.5 km^2 (3.5×7 km^2 prior to August 6, 2019), respectively. As summarized in Table 1, we used the OMI QA4ECV version 1.1 product (Boersma et al., 2017, 2018) for April–August 2016 and May–August 2018, and the TROPOMI version 2.4 reprocessing product (Copernicus Sentinel-5P (processed by ESA), 2021; van Geffen et al., 2022) for May–August 2018.

These products were retrieved using the differential optical absorption spectroscopy (DOAS) approach within the 405–465 nm wavelength window. Slight differences in the detailed retrieval settings existed between OMI and TROPOMI, including the formulation of modeled reflectance, fitting methods, and intensity offset correction (van Geffen et al., 2020). Other differences are the surface reflectance input (TROPOMI DLER versus OMI LER) and the cloud retrieval (TROPOMI FRESCO O-2A band versus OMI O2-O2 cloud retrievals). In addition to the OMI row anomaly, the TROPOMI slant column density (SCD) error in 2018 was approximately 40% lower than that of OMI (van Geffen et al., 2020). The tropospheric NO_2 vertical column density (VCD) was derived using air mass factors (AMFs) and *a priori* profiles.

For OMI retrievals, the following screening criteria were applied: cloud radiance fraction (CRF) < 0.5, solar zenith angle (SZA) $< 81^\circ$, surface albedo < 0.3, quality flag $= 0$, and a ratio of tropospheric AMF to geometric AMF > 0.1. Retrievals affected by row anomalies were excluded using quality flags. TROPOMI retrievals were used if they had quality assurance (QA) values > 0.75, which correspond to good-quality retrievals over (nearly) cloud-free scenes and is similar to the OMI screening criteria.

2.2.2 OMI and TROPOMI SO_2 column

We used OMI V2 SO_2 PCA (OMSO2 V2) data (Li et al., 2020a, b) spanning the periods from April to August 2016 and from May to August 2018. OMI SO_2 VCDs were calculated using a constant air mass factor of 0.36. The observation error was set to be a constant value of 0.25 DU due to the lack of error information. We used OMI SO_2 data with a cloud radiance fraction of $<$20% and solar zenith angles of $<70^\circ$, while excluding the first 10 and last 10 cross-track positions to limit across-track pixels, following Fioletov et al. (2016, 2017).

The TROPOMI SO_2 Covariance-Based Retrieval Algorithm (COBRA) version 2 product (Theys et al., 2021) was used for the period of May–August 2018. The COBRA approach corrects most artifacts in the DOAS SO_2 SCD and reduces noise and biases in the operational TROPOMI DOAS SO_2 product. The systematic VCD uncertainty (from the COBRA spectral fit) was

https://doi.org/10.5194/egusphere-2026-1681
Preprint. Discussion started: 27 April 2026

typically less than 0.04 DU, while the VCD precision for individual pixels ranged from 0.5 to 1 DU (Theys and Vlietinck, 2024). Retrievals with QA values > 0.5 were used. We additionally applied the following criteria: the data with SZA $> 65°$ and VCD $<$ -0.045 μmol m^{-2}, snow flag $= 1$, AMF < 0.15, selected window flag $= 3$, CRF > 0.5, and sulfur dioxide COBRA flag $= 0$ or 1 were excluded according to Theys and Vlietinck (2024). Most of the data with selected window flag $= 2$ were also excluded by multiplying 0.6 to the QA values.

2.2.3 MODIS and VIIRS AOD

MODIS and VIIRS are passive multi-wavelength imaging radiometers (Barnes et al., 1998; Cao et al., 2013), on board the Terra and Aqua satellites and the Suomi-NPP and NOAA-20 satellites, respectively. For MODIS, we used the aerosol 5-min L2 Swath 10 km Collection 6.1 (MOD04_L2 and MYD04_L2) products (Levy et al., 2017), in which three different algorithms are applied for aerosol retrievals over diverse surface types. The Dark Target (DT) ocean and land algorithms (Levy et al., 2015) were used over the ocean, vegetated, and dark soil areas, whereas the Deep Blue (DB) algorithm (Sayer et al., 2015) was applied over brighter surfaces (e.g., deserts, barren rocks, urban areas, and vegetated regions). We used the "Optical_Depth_Land_And_Ocean" dataset, which merges DT- and DB-retrieved AOD with reference to quality assurance and confidence (QAC) values (Levy et al., 2013).

For VIIRS, we used the Deep Blue Aerosol L2 6-min Swath 6 km version 2 (AERDB_L2_VIIRS_SNPP and AERDB_L2_VIIRS_NOAA20) products (Lee et al., 2024). The AOD product was retrieved using the DB algorithm (Hsu et al., 2019) over land and the Satellite Ocean Aerosol Retrieval (SOAR) algorithm (Sayer et al., 2018) over the ocean. These products were generally consistent with the MODIS DB products for long-term satellite AOD records (Hsu et al., 2019). The algorithm updates in the version 2 products, including better accounting for effects of surface pressure, improved determination of surface reflectance, and the inclusion of fine-mode aerosol optical models, improved the agreements with the ground-based remote sensing (AERONET) over land (Lee et al., 2024). For assimilation, we used the "Aerosol_Optical_Thickness_550_Land_Ocean_Best_Estimate" data fields.

The expected errors of MODIS AOD products were reported by Remer et al. (2005) as $\pm 0.03 \pm 0.05\tau$ over the ocean, and $\pm 0.05 \pm 0.15\tau$ over the land. In this study, observation errors for assimilation were reassigned using a formulation that assigns errors as a function of the scattering angle at the pixel level, following Benedetti et al. (2009). For observations over the ocean, measurement errors were calculated as follows:

$$\epsilon_{\tau_o} = max(0.02, \tau_o(0.007 + 0.0012 \times \Theta) + 0.001), \tag{7}$$

where τ_o represents the AOD retrievals over the ocean and Θ denotes the scattering angle. For observations over the land, measurement errors were calculated as follows:

$$\epsilon_{\tau_l} = max(0.02, 0.5\tau_l), \tag{8}$$

where τ_l represents the AOD retrievals over the land. An additional 5% error was added to account for representativeness errors.

https://doi.org/10.5194/egusphere-2026-1681
Preprint. Discussion started: 27 April 2026

An additional filtering approach proposed by Hyer et al. (2011) was applied. We filtered out the data using the following criteria: QAC value < 3, cloud fraction > 0, scattering angle $> 170°$, absence of adjacent retrievals, fewer than five retrievals within the model grid, and cases where the ratio of the standard deviation of AOD to the mean AOD within the model grid was greater than 0.5, specifically when the mean AOD was smaller than 0.2. The following criteria were applied to the VIIRS AOD data to filter out the data with low quality: QA flag < 3, scattering angle $>170°$, absence of adjacent retrievals, fewer than five retrievals within the model grid, and cases where the ratio of the standard deviation of AOD to the mean AOD within the model grid was greater than 0.5, specifically when the mean AOD was smaller than 0.2. After filtering, the mean AOD at the 1.1° model grid was calculated using a grid-averaging approach, as pixel corner location information was unavailable.

2.2.4 MOPITT CO column

CO column observations were obtained from the Measurement of Pollution in the Troposphere (MOPITT) V7 TIR-NIR (thermal infrared and near-infrared) multispectral L2 products (Deeter et al., 2017). The local equator crossing time was 10:40LT. The overall retrieval biases, bias variability, and drift in the V7 product were improved compared with those in the V6 product. Retrievals in polar regions (>65° N/S) were excluded due to potential problems related to cloud detection and snow/ice surfaces. Nighttime data were filtered out using SZA, as daytime conditions generally provide better thermal contrast for the retrievals. The retrieval error was adopted as the observation error during the analysis step.

2.2.5 MLS ozone and HNO_3 profiles

Microwave Limb Sounder (MLS) v4.2 L2 products (Manney et al., 2015; Schwartz et al., 2015) were used for ozone and HNO_3 profiles above 220 hPa. The local equator crossing time was 13:40LT. The measurement accuracy and precision were adopted as the observation error, estimated at 30–60 ppbv and 20–200 ppbv for ozone, respectively, and 0.6 ppbv and 1.0–1.1 ppbv for HNO_3, in the lower stratosphere (Livesey et al., 2011).

2.3 Super-observation approach

The state-of-the-art super-observation approach developed by Rijsdijk et al. (2025) was applied to TROPOMI NO_2, SO_2, and OMI NO_2. To generate satellite observations representative of the model grid size (1.1°), individual tropospheric NO_2 VCDs were averaged together with their corresponding averaging kernel values. A weighting function based on the overlap between satellite pixels and the model grid was used for the averaging. The total super-observation uncertainty (σ_s) was estimated from the measurement error (σ_{obs}) and representativity error (σ_{RE}):

$$\sigma_s = \sqrt{\sigma_{obs}^2 + \sigma_{RE}^2}.$$

The measurement error term is calculated as a combination of the uncorrelated and correlated parts of individual uncertainty components with a representative correlation factor (c) for stratospheric, SCD, and AMF uncertainties:

$$\sigma_{obs}^2 = (1-c)\sum_{i=1}^{N} w_i^2\sigma_i^2 + c(\sum_{i=1}^{N} w_i\sigma_i)^2,$$

https://doi.org/10.5194/egusphere-2026-1681
Preprint. Discussion started: 27 April 2026

where w_i is the area overlap between the satellite pixels and the selected model grid, and σ_i represents the uncertainty of the individual components. The correlated component decreases, while the uncorrelated component remains unchanged, as the number of observations increases. The representativity error term was estimated as a function of standard deviation within a model grid, the total population size of fractional observations, and coverage area fractions (Eq. 18 of Rijsdijk et al. (2025)), with modification to consider systematic data gaps in observation coverages, for example, those caused by the presence of clouds. For polluted cases, the representativity errors, when estimated by accounting for systematic deficiencies, were more than twice as large at 10–90% area-coverage fractions compared to those estimated using a random-deficiency approach in our previous studies.

A super-observation approach, similar to that used for NO_2, was applied to the TROPOMI COBRA SO_2 product. The total super-observation uncertainty was estimated in a manner consistent with the NO_2 case. The measurement error term was calculated as a combination of random and systematic uncertainties when applying the averaging kernels. The representativity error term for SO_2 was estimated using the same formula as that for NO_2 without modification for the systematic data gaps in observation coverage and with a correction for the measurement noise in the calculation of the representativity error by subtracting the associated random uncertainty from the total super-observation uncertainty. The representativity errors for SO_2 were 80% and 72% smaller than those for NO_2 under both clean and polluted conditions, respectively. These results were consistent with the fact that SO_2 column is less heterogeneous than tropospheric NO_2 column, reflecting longer atmospheric lifetime of SO_2 ($\approx$20 to 60 hours) (Lee et al., 2011).

For OMI SO_2 and MOPITT CO, the conventional super-observation approach was applied as in (Miyazaki et al., 2019, 2020a).

2.4 Data assimilation experiments

Figure 1 and Table 2 summarize the data assimilation experiments and model simulations performed in this study. To evaluate the relative importance and synergetic effects of trace gases and AOD DA, we conducted three DA experiments: "GasAero", which simultaneously assimilated trace gas (e.g., NO_2, SO_2) and AOD observations; "Gas-only", which assimilated trace gas observations only; and "Aero-only" which assimilated AOD observations only. The time period April–August 2016 was selected because of photochemically active season, which covers the NASA's KORUS-AQ aircraft-campaign observations.

Furthermore, to assess the impact of improved constraints from the current generation satellites through improved accuracy and coverage compared to the previous generation satellites, we evaluated the relative performance using different sets of satellite observations: "OMI+MODIS" assimilated trace gas observations from Aura/OMI and AOD observations from Terra+Aqua/MODIS, and "TROPOMI+VIIRS" assimilated trace gas observations from Sentinel-5P/TROPOMI and AOD observations from Suomi-NPP+NOAA-20/VIIRS. The assimilation period of May–August 2018 was selected because of the similar season to those in 2016, while TROPOMI data were available after May 2018.

To evaluate the impacts of individual assimilation runs, control simulations "CTL" without any data assimilation were conducted for 2016 and 2018 using *a priori* emission data.

https://doi.org/10.5194/egusphere-2026-1681
Preprint. Discussion started: 27 April 2026

2.5 Observations for the validation

2.5.1 AERONET ground-based remote sensing network

We assessed the performance of both the data assimilation and the control simulations using ground-based observations from the Aerosol Robotic Network (AERONET) (Holben et al., 1998). We used aerosol optical depth (AOD) at 500 nm derived from AERONET version 3 retrievals (Sinyuk et al., 2020). AOD for May–August 2016 at 181 sites and for June–August 2018 at 179 sites, which cover more than 25% of the target periods, were used for validation. The typical uncertainty of AERONET AOD at visible wavelengths is about 0.01 (Holben et al., 1998).

2.5.2 Surface in-situ observation networks

We used near-surface in-situ observations of sulfate, nitrate, and ammonium aerosols from multiple regional monitoring networks: the European Monitoring and Evaluation Programme (EMEP; https://ebas.nilu.no, last access: May 21, 2025) for Europe, the Clean Air Status and Trends Network (CASTNET; https://www.epa.gov/castnet, last access: May 21, 2025) for the United States, and the Acid Deposition Monitoring Network in East Asia (EANET; https://www.eanet.asia, last access: May 21, 2025) for East Asia. For validation, we selected data from rural, remote, and background sites (41, 80, and 15 sites from EMEP, CASTNET, and EANET, respectively) and excluded urban sites, as the coarse model grid resolution cannot adequately capture urban-scale pollution. Typical uncertainties are estimated to be 3% for sulfate, 8% for nitrate, and 4% for ammonium and detection limits for sites are 0.07 μg m^{-3} for sulfate, 0.04 μg m^{-3} for nitrate, and 0.06 μg m^{-3} for ammonium in the eastern United States (Sickles and Shadwick, 2002).

Near-surface $PM_{2.5}$ in-situ observations were obtained from the Air Quality (AQ) e-reporting products of the European Environment Agency (EEA; https://eeadmz1-downloads-webapp.azurewebsites.net, last access: May 22, 2025) for Europe, the Air Quality System (AQS; https://www.epa.gov/aqs, last access: May 22, 2025) for the United States, and national monitoring networks in Japan (https://tenbou.nies.go.jp/download, last access: May 22, 2025) and South Korea (AirKorea; https://airkorea.or.kr, last access: May 22, 2025) for Northeast Asia. The observation data were derived from 188, 790, and 1204 sites in the EEA AQ e-reporting products, AQS, and Japanese and Korean networks, respectively. The continuous $PM_{2.5}$ measurements typically differ from filter-based measurements by less than 10% (Chow et al., 2006).

2.5.3 NASA's KORUS-AQ and ATom-4 aircraft-campaign observations

We also used aircraft observations from the Korea–United States Air Quality campaign (KORUS-AQ; Crawford et al. 2021) and the Atmospheric Tomography Mission phase 4 (ATom-4; Wofsy et al. 2018). The validation focused on sulfate, nitrate, and ammonium aerosols, aerosol extinction coefficients, and related gas-phase species (NO_2, SO_2, HNO_3, and OH). Sulfate, nitrate, and ammonium aerosols smaller than 1 μm in diameter were measured with the aerosol mass spectrometer (AMS; DeCarlo et al. 2006). Concentrations of SO_2 and HNO_3 were measured using the chemical ionization mass spectrometer (CIMS; Crounse et al. 2006), while NO_2 was derived from the 4-channel $NO_{xy}O_3$ chemiluminescence instrument (Weinheimer

https://doi.org/10.5194/egusphere-2026-1681
Preprint. Discussion started: 27 April 2026

et al., 1993). OH concentrations were measured by Airborne Tropospheric Hydrogen Oxides Sensor (ATHOS) (e.g., Miller and Brune, 2022). For KORUS-AQ, we used data from 20 flights conducted between May 1 and June 9, 2016, and for ATom-4, from four flights between May 17 and 21, 2018. Typical uncertainties are estimated to be 35% for inorganic aerosols, 100 pptv + 30% for NO_2, 30% for SO_2, and 30% for HNO_3, and 74% for OH (Bahreini et al., 2009; Kim et al., 2022).

3 Aerosol analysis results

3.1 Relative impacts of AOD and trace gas observations

As shown in Figs. 2 and 3, GasAero DA decreased surface mass concentrations of sulfate aerosols by 9–44% relative to the control simulation over most regions, except for South America and North Africa. Gas-only and Aero-only DA runs demonstrate the relative importance of AOD and trace gas observations. The Gas-only DA reduced sulfate aerosols by 20–56% over most regions, except for South America. These reductions were partially offset by corrections in the Aero-only DA (typically 11–31%). These results demonstrate the independent constraints provided by AOD and trace gas observations, which act to increase total aerosols and decrease sulfate aerosols, respectively.

The combined GasAero DA reduced nitrate aerosol concentrations over India and Central Africa by 4–64%, while increasing them in polluted regions by 48–80%. The conventional Gas-only and Aero-only DA experiments further demonstrate that the impacts of trace gas observations were increases in nitrate aerosols by a factor of 1.5–5 over eastern China, the eastern United States, Europe, North and South Africa, and the Middle East, while decreasing them by 2–61% over Southeast Asia, India, Central Africa, and South America. The impacts of AOD observations were reductions in nitrate aerosols over the eastern United States, Europe, Southeast Asia, India, North Africa, and South America by 14–51%. These results suggest that optimization for NO_x emissions plays a dominant role in nitrate analysis compared to the AOD assimilation in most regions, except for India.

Ammonium aerosol concentrations decreased by up to 44% due to the combined GasAero DA, primarily due to a lower partitioning ratio of particulate-phase ammonium to gas-phase ammonia as a result of changes in sulfate and nitrate aerosols. Gas-only DA reduced concentrations over most regions by 5–56%. In contrast, Aero-only DA increased ammonium aerosols over eastern China, Southeast Asia, North Africa, and the Middle East by 8–41%, while reducing them over the eastern United States, India, Central and South Africa, South America by 4–43%. These results show that the AOD observations are constraining the total aerosol amount, but are unaware of the partitioning of ammonium, which is similar to the sulfate analysis. Furthermore, an optmization of NH_3 emissions based on CrIS satellite observations leads to increases in nitrate and ammonium aerosols (Fig. S2), whereas optimized NH_3 emissions have no significant impact on sulfate ($<2\%$).

With GasAero DA, total $PM_{2.5}$ concentrations were modified both through direct constraints from AOD and indirect constraints from trace gases via changes in secondary aerosol production. As a result, GasAero DA increased $PM_{2.5}$ by 7–59% over China, Europe, the United States, and Southeast Asia, while decreasing them by 2–49% over India, biomass-burning regions, and arid regions. The Aero-only DA increased $PM_{2.5}$ over eastern China, the eastern United States, Europe, and Southeast

https://doi.org/10.5194/egusphere-2026-1681
Preprint. Discussion started: 27 April 2026

Asia by 11–71%, but decreased over India, Africa, South America, and the Middle East by 2–46%. In contrast, the Gas-only DA reduced $PM_{2.5}$ over most regions by up to 15%.

Overall, the results suggest that corrections to sulfate, nitrate, and ammonium from assimilating trace gas observations were generally larger than those from AOD assimilation over most regions, except for North and South Africa where uncertainties in aerosol formation, transport, and deposition processes (e.g., heterogeneous reactions on primary aerosols) may be larger than those in precursor gas emissions. In contrast, corrections in $PM_{2.5}$ total mass were dominated by Aero-only DA.

3.2 Validation using AERONET observations

As shown in Fig. 4 and Table 3, compared to AERONET observations, the mean model AOD bias was 0.01 (4%) in the control model simulation. However, biases at individual sites largely varied. Correlation coefficient and RMSE between the observed and simulated AOD at different sites were 0.78 and 0.11, respectively. GasAero DA shows a mean bias of -0.04 (-21%), whereas the correlation coefficient was improved to 0.90. RMSE was also reduced by 36% due to GasAero DA. Negative biases were larger in areas with high aerosol concentrations, such as East Asia, South Asia, the Middle East, and the Saharan Desert. This could be attributed to unresolved enhancement of AOD in the coarse-resolution model. The negative mean bias in the Gas-only DA was larger than that in the GasAero DA, while the correlation coefficient degraded to 0.67 and the RMSE increased by 85%. This result can be explained by constraining part of the aerosol composition from the Gas-only DA. In contrast, the Aero-only DA exhibited a smaller negative bias than the GasAero DA, with correlation coefficients and RMSE values comparable to those in the GasAero DA.

3.3 Validation using KORUS-AQ observations

Figure 5 compares the vertical profiles of sulfate, nitrate, and ammonium aerosols, aerosol extinction coefficients, and the related gas-phase species (SO_2, NO_2, HNO_3, and OH). The CTL experiment overestimated sulfate aerosols across all vertical layers, with a positive bias of 1.57 μg m^{-3} (by 36%) in the lower troposphere (below 750 hPa), where the GasAero DA largely removed this bias (Table 3). In the lower troposphere, the remaining bias and RMSE in the GasAero DA were 6–98% smaller than those in the Gas-only DA and Aero-only DA. These results indicate that both trace gas and AOD observations contributed to reducing the sulfate aerosol biases.

The CTL simulation underestimated nitrate and ammonium aerosols in the lower troposphere by 1.24 and 0.24 μg m^{-3}, respectively (-44% and -10%, respectively), while both species were overestimated in the free troposphere. In the GasAero DA, the negative model biases of nitrate and ammonium aerosols in the lower troposphere shifted to positive biases of 0.74 and 0.07 μg m^{-3}, respectively (26% and 3%, respectively), whereas their positive biases in the free troposphere increased. The improvements in nitrate aerosol biases in the lower troposphere were primarily attributed to the Gas-only DA. Conversely, the RMSE for nitrate aerosols in the lower troposphere in Aero-only DA was 8–13% smaller than that in GasAero and Gas-only DA. Positive model biases in nitric acid can lead to positive nitrate biases in the free troposphere through nitrate aerosol formation, which could partially be attributed to missing sinks in the forecast model, such as particulate nitrate photolysis (e.g.,

https://doi.org/10.5194/egusphere-2026-1681
Preprint. Discussion started: 27 April 2026

Shah et al., 2024). For ammonium aerosols, both bias and RMSE in the lower troposphere in the GasAero DA were 3–88% smaller than those in Gas-only and Aero-only DAs due to improvements in sulfate and nitrate aerosols.

CTL also underestimated the total extinction coefficients in the lower troposphere by 0.074 km^{-1} (by -69%), whereas the GasAero DA reduced it by 15%. The bias reduction in the extinction coefficients were dominated by Aero-only DA.

The mean biases of SO_2 and HNO_3 in the CTL were positive by 64% and 28%, respectively, whereas that of NO_2 was negative by 62% in the lower troposphere. The biases of SO_2 and NO_2 were reduced by 41% and 47%, respectively, in the GasAero DA. The improvements were primarily attributable to the Gas-only DA, but the Aero-only DA also influenced the performance through OH changes driven by a combination of non-linear chemistry and heterogeneous HO_2 uptake on aerosols. In contrast, the positive bias of HNO_3 in the CTL increased by a factor of 3.6 in the GasAero DA. These results suggest that the positive HNO_3 bias originated from formation and deposition processes, such as wet scavenging (Luo et al., 2019), rather than from NO_x emissions.

3.4 Validation using surface observations

3.4.1 The United States

As summarized in Fig. 6 and Table 3, over the United States, the CTL simulation overestimated sulfate aerosols by 0.20 $\mu g\ m^{-3}$ (by 17.2%) compared to CASTNET, with particularly large positive biases over the eastern United States, because of positive biases in the *a priori* SO_2 emissions and uncertainties in the sulfate formation and scavenging processes in the forecast model. In contrast, the GasAero DA showed the negative bias of 0.03 $\mu g\ m^{-3}$ (by -2.3%) relative to CASTNET across the United States. The spatial correlation coefficient increased from 0.59 to 0.65, while the RMSE for sulfate aerosols decreased by 31%. Sulfate aerosol bias in the Gas-only DA became negative by 0.13 $\mu g\ m^{-3}$, which was 35% smaller than the CTL, whereas the Aero-only DA degraded this bias by a factor of 1.5. Spatial correlation coefficients in the GasAero, Gas-only, and Aero-only DA were comparable, while RMSEs in tne GasAero and Gas-only DA were 31% smaller than those in the Aero-only DA. The performance on sulfate concentrations in the GasAero DA were better than those in the Gas-only and Aero-only DA rus.

Nitrate aerosols were underestimated by CTL by 0.14 $\mu g\ m^{-3}$ (by -42.6%) particularly over the central United States and along the eastern and western coasts. In the GasAero DA, the nitrate bias became positive bias of 0.05 $\mu g\ m^{-3}$ (by 14.3%), while the spatial correlation coefficient increased from 0.37 to 0.44 and the RMSE for nitrate aerosols decreased by 4%. The nitrate aerosol bias and RMSE in the GasAero DA were up to 77% smaller than those in the Aero-only DA, but up to 67% larger than those in the Gas-only DA. The spatial correlation coefficient in the Aero-only DA was the highest among the three DA experiments.

CTL also overestimated ammonium aerosols by 0.03 $\mu g\ m^{-3}$ (by 7.3%), particularly over the eastern United States. The positive model bias was reduced by 83% to 0.005 $\mu g\ m^{-3}$ (by 1.2%) in the GasAero DA, while the correlation coefficient remained unchanged. The RMSE for ammonium aerosols was also reduced by 20% in the GasAero DA. The ammonium aerosol bias in the GasAero DA was 75% smaller than that in both the Gas-only and Aero-only DA. The correlation coefficients and RMSEs for ammonium aerosols were comparable across the GasAero, Gas-only, and Aero-only DA runs.

https://doi.org/10.5194/egusphere-2026-1681
Preprint. Discussion started: 27 April 2026

$PM_{2.5}$ total mass concentrations were substantially underestimated in the CTL simulations relative to AQS observations across most parts of the United States, with a negative mean bias of 1.75 μg m^{-3} (by -44.7%). GasAero DA reduced this bias by more than 70% to -0.46 μg m^{-3} (by -16.0%), while the correlation coefficient improved markedly from 0.46 to 0.80. The RMSE for $PM_{2.5}$ decreased by about 50%. The negative bias reductions in the GasAero DA were more evident over the eastern United States than those over the western United States, except for the eastern coastal areas where negative biases shifted to positive biases. This feature in spatial pattern was similar to that achieved in the Aero-only DA, but more pronounced than in the Gas-only DA.

3.4.2 Europe

In Europe, the CTL simulation overestimated sulfate aerosols relative to EMEP observations by 1.09 μg·m^{-3} (by 253%), with the largest positive biases occurring in the United Kingdom, Germany, and eastern Europe (Fig. 7). GasAero DA reduced the positive bias by 20% to 0.87 μg m^{-3} (by 202%) and decreased RMSE by a similar magnitude, although the correlation coefficient decreased from 0.37 to 0.13. The bias and RMSE in Gas-only DA were 9–35% smaller than those in GasAero and Aero-only DA, whereas the correlation coefficient in Aero-only DA was higher than in both GasAero and Gas-only DA. These results suggested that sulfate model biases at individual sites in Europe were influenced by not only precursor emissions but also aerosol formation, transport, and deposition processes.

Mean biases of nitrate and ammonium aerosols in CTL were positive (by 9.1%) over parts of Germany and Poland. For nitrate aerosols, the positive model bias increased to 0.22 μg m^{-3} (by 83.3%) due to the GasAero DA, while the correlation coefficient remained nearly unchanged and the RMSE increased by 53%. Compared with the GasAero and Gas-only DA runs, the Aero-only DA produced smaller nitrate aerosol biases and RMSE values.

For ammonium aerosols, the small positive bias of 0.01 μg m^{-3} (by 2.0%) in CTL shifted to a slight negative bias of 0.014 μg m^{-3} (by -2.8%) after the GasAero DA, while these biases were less than typical measurement errors. The correlation coefficient improved marginally from 0.40 to 0.41, and the RMSE was reduced by 10%. The statistical scores were comparable across the GasAero, Gas-only, and Aero-only DA runs.

The $PM_{2.5}$ total mass concentrations in CTL were underestimated by 1.71 μg m^{-3} (by -45.8%), particularly over northern Italy and Czech Republic. The GasAero DA reduced the negative model bias of $PM_{2.5}$ by 12% to -1.51 μg m^{-3} (by -40.6%), whereas the correlation coefficient decreased from 0.15 to 0.13. The RMSE for $PM_{2.5}$ remained nearly constant after the GasAero DA. Smaller improvements in $PM_{2.5}$ over Europe than the United States reflected less numbers of assimilated AOD observations over areas with large negative biases.

3.4.3 East Asia

As shown in Fig. 8, the CTL simulation overestimated sulfate aerosols compared to EANET by 0.63 μg m^{-3} (by 27.6%). The positive model bias was shifted to negative bias of 0.14 μg m^{-3} (by -6.4%) by the GasAero DA. The correlation coefficient decreased from 0.83 to 0.77 with the GasAero DA, whereas RMSE was reduced by 29%. The bias and RMSE in the GasAero

https://doi.org/10.5194/egusphere-2026-1681
Preprint. Discussion started: 27 April 2026

DA were 7–78% smaller than those in the Gas-only and Aero-only DA, while the correlation coefficient in the Aero-only DA was higher than that in both the GasAero and Gas-only DA experiments.

In contrast, the CTL simulation underestimated nitrate aerosols by 0.37 μg m^{-3} (by -64.5%), except over Cheju Island, South Korea. The negative model bias was reduced by 59% to 0.15 μg m^{-3} (by -26.4%) with the GasAero DA. The correlation coefficient for nitrate aerosols decreased from 0.39 to 0.36, whereas the RMSE was reduced by 9%. The improvements in nitrate aerosols from the GasAero DA were primarily driven by the Gas-only DA.

Ammonium aerosols were overestimated in CTL by 0.05 μg m^{-3} (by 12.7%). The positive model bias was mostly removed by the GasAero DA. The correlation coefficient improved from 0.58 to 0.61 with the GasAero DA, while the RMSE was reduced by 5%. The bias in the GasAero DA was 97% smaller than that in both the Gas-only and Aero-only DAs, whereas the correlation coefficient and RMSE in the Aero-only DA were superior.

Mean biases of $PM_{2.5}$ total mass concentrations were negative by 1.42 μg m^{-3} (by -9.9%). With the GasAero DA, the negative model bias shifted to positive bias of 1.13 μg m^{-3} (by 7.9%), while the correlation coefficient improved from 0.70 to 0.82. The RMSE for $PM_{2.5}$ remained nearly constant. The $PM_{2.5}$ bias and RMSE were 14–74% smaller than those in the Gas-only and Aero-only DA runs.

Overall, these results demonstrate the benefits of the combined use of satellite trace gas and AOD observations across many regions. Data assimilation increments of sulfate and ammonium aerosols made by satellite trace gas and AOD observations were negative and positive, respectively, probably because the forecast model has different biases in aerosol formation from precursor gases and in transport and deposition processes. The combined assimilation showed the best performance for many cases. This finding suggests that comprehensive constraints on precursor emissions, formation, transport, and deposition processes are needed to improve aerosol composition analyses.

4 Emission estimates

4.1 Relative impacts of satellite AOD and trace gas observations

The obtained changes in the aerosol concentration analysis were largely attributed to changes in emissions. The developed DA system provided top-down estimates for carbonaceous and soil dust emissions, as well as for SO_2 and NO_x emissions. As summarized in Table 4, the global total emissions of carbonaceous aerosols increased by 15% in the GasAero DA relative to the *a priori* emissions. On regional scales, the estimated emissions over China and Southeast Asia increased by factors of 3.0 and 2.6, respectively, compared to the *a priori* emissions, whereas the emissions over India decreased by 22%. These emission corrections made by the GasAero DA were mainly driven by, but slightly larger than, those made by the Aero-only DA, demonstrating the importance of AOD observations in constraining primary aerosols. The slight differences between the GasAero and Aero-only DA runs were due to small AOD reductions in most regions resulting from the assimilation of trace gas observations.

The GasAero DA reduced the global total soil dust emissions by approximately 60% relative to the *a priori* emissions predicted by the forecast model. Regionally, soil dust emissions decreased considerably in the Gobi and Taklamakan Deserts

https://doi.org/10.5194/egusphere-2026-1681
Preprint. Discussion started: 27 April 2026

in China and in the Thar Desert in India (Fig. 9). Dust emissions also decreased in parts of the Balkan Peninsula and the Sahara Desert. These corrections made by the GasAero DA were largely driven by the Aero-only DA, similar to the case of carbonaceous aerosols.

The global total SO_2 emissions were reduced by approximately 30% in the GasAero DA relative to the *a priori* emissions. Large negative emission increments ($>4 \times 10^{-11}$ kg S m^{-2} s^{-1}) were found in industrialized regions, including eastern China, northern India, eastern Europe, and the eastern United States, suggesting substantial overestimations in the *a prior* emission inventories. These corrections made by the GasAero DA were primarily attributable to the Gas-only DA.

The GasAero DA increased the global total NO_x emissions by 30%. On regional scales, the *a posterior* emissions over most areas increased by 33–80%, except in South America and Central Africa. The emission increases can be attributed to soil NO_x emissions by 30–75% over China, the United States, and Europe. These emission corrections in the GasAero DA were slightly larger than those in the Gas-only DA. The additional modifications introduced by AOD observations are likely related to their impacts on NO_x lifetime through heterogeneous reactions on aerosols during the forecast steps.

4.2 Comparison with other estimates

We also compared the *a priori* (CEDS v2021_04_21+GFEDv4.1s) and *a posteriori* emissions with the most recent bottom-up emission inventories, including HTAPv3.2 (Guizzardi et al., 2025) and GFED5 (Chen et al., 2023). The HTAPv3.2 inventory harmonizes the EDGARv8 global anthropogenic emission inventory (Crippa et al., 2024) with regional and national inventories from Canada, Europe, the United States, China, Korea, Japan, and other Asian countries. The GFED5 inventory represents the latest global biomass burning emissions, derived from long-term burned area records from MODIS, with further refinements based on high-resolution satellite observations such as Landsat and Sentinel-2.

Compared to the HTAPv3.2 and GFED5 inventories (59.7 Tg/yr), the global *a posteriori* carbonaceous aerosol emissions (103.3 Tg/yr) were approximately twice as large, with large differences over boreal forest, eastern China, and Central Africa (Fig. S3). However, the emission estimates in this study fall within the range of other top-down estimates (100–166 Tg/yr) (Huneeus et al., 2012; Schutgens et al., 2012; Chen et al., 2019, 2022; Tsikerdekis et al., 2023), which assumed an OA-to-OC ratio of 1.4. The large discrepancies between the bottom-up inventories and top-down estimates may reflect uncertainties in emission factors and activity data for region-specific sources such as motorcycles, kerosene use, open waste burning, and ad hoc oil refining in Africa (Liousse et al., 2014; Marais and Wiedinmyer, 2016) and large uncertainties in biomass burning emissions (Hua et al., 2024), as well as uncertainties in the modeled relationships between AOD and aerosol concentrations (Gliß et al., 2021) in our top-down estimates.

The estimated global dust emissions (1257 Tg/yr) were within the range of 731–1536 Tg/yr based on satellite observations (e.g., Ginoux et al., 2012; Chen et al., 2019; Tsikerdekis et al., 2023) and the multi-model estimates of 1130–4311 Tg/yr from the AeroCom-III models (Kim et al., 2024). However, our estimate is lower than the latest DustCoMMv1 dust emission estimate of 2148 Tg/yr (Leung et al., 2025). The limited temporal coverage of this study (i.e., May–August 2016) could partly account for the differences relative to annual emission rates.

https://doi.org/10.5194/egusphere-2026-1681
Preprint. Discussion started: 27 April 2026

Compared to the HTAPv3.2 and GFED5 emission inventories (41.0 Tg S/yr), the *a posteriori* SO_2 emissions (29.6 Tg S/yr) were smaller, particularly over China and India (Fig. S3). These results suggest that bottom-up emission inventories may be overestimated. However, the estimated SO_2 emissions resulted in negative biases in near-surface SO_2 concentrations compared to the KORUS-AQ aircraft campaign observations (Fig. 5), as also reported by Miyazaki et al. (2019). Our top-down SO_2 estimates may involve substantial uncertainties arising from retrieval errors, assumed observation-error statistics, assumptions related to the air mass factor (AMF) in the data assimilation system, and uncertainties in model processes such as dry deposition (Luo et al., 2020; Hardacre et al., 2021). These factors should be carefully considered to interpret the differences.

The *a posteriori* NO_x emissions (63.6 Tg N/yr) were closer to the combined HTAPv3.2, GFED5, and CAMS-GLOB-SOIL inventories (Simpson et al., 2023) (56.8 Tg N/yr) than the *a priori* emissions in most regions, except for Southeast Asia and North and Central Africa (Fig. S3). These results suggest overall improvements in NO_x emission estimates through data assimilation.

5 Impacts of current and previous generation satellites

Advanced satellite retrievals derived from TROPOMI and VIIRS, which are successors to OMI and MODIS, respectively, have became available and improved tropospheric NO_2 data assimilation performance (Sekiya et al., 2022). However, their value for aerosol composition analysis remains unclear. As shown in Fig. 10, the TROPOMI+VIIRS DA produced smaller decreases and increases in sulfate aerosols over eastern China and South America (-45% and $+11\%$, respectively) compared to the OMI+MODIS DA (-55% and $+24\%$, respectively). The increases in nitrate aerosols over eastern China caused by the TROPOMI+VIIRS DA were 50% smaller, whereas the increases over the ocean were larger. For ammonium aerosols, the two DA cases produced spatial correction patterns similar to those for sulfate aerosols. The TROPOMI+VIIRS DA resulted in a 45% $PM_{2.5}$ increase over North Africa, in contrast to a 5% decrease with the OMI+MODIS DA. In addition, the TROPOMI+VIIRS DA produced smaller increases (by 16%) and decreases (by -1%) in $PM_{2.5}$ over eastern China and India, respectively, compared to the OMI+MODIS DA (48% and -30%).

As summarized in Table 5, the CTL run underestimated the AOD derived from AERONET by 0.043 (-22%). The correlation coefficient and RMSE for mean AOD during June–August 2018 were 0.66 and 0.1, respectively. The TROPOMI+VIIRS DA reduced the negative AOD model bias and RMSE by 93% and 39%, respectively, while the correlation coefficient was improved to 0.83. In the OMI+MODIS DA the model bias and RMSE were also reduced by 63% and 14%, respectively, while the correlation coefficient was comparable to that in the CTL run. The improvements in AOD due to the TROPOMI+VIIRS DA were larger than those due to the OMI+MODIS DA, which is particularly evident over South Africa, India, and Sahel regions (Fig. S4). These improvements can be attributed to the VIIRS DB algorithm updates (Lee et al., 2024).

In the CTL run, sulfate aerosols exhibited positive model biases of 0.20–0.73 $\mu g\ m^{-3}$ (12–131%) and RMSEs of 0.64–0.94 $\mu g\ m^{-3}$ (46–333%) against independent observations (EMEP, CASTNET, EANET, and NASA's ATom-4), with correlation coefficients of 0.04–0.72. The TROPOMI+VIIRS DA reduced sulfate biases relative to EMEP, CASTNET, and ATom-4 to 0.11–0.53 $\mu g\ m^{-3}$ (10–96%), while the positive bias against EANET shifted to a negative bias of $\breve{}0.19\ \mu g\ m^{-3}$ (by -10%).

https://doi.org/10.5194/egusphere-2026-1681
Preprint. Discussion started: 27 April 2026

RMSEs were reduced by 2–21%. Spatial correlation coefficients were improved by 0.01–0.08 for CASTNET and EANET but decreased by 0.05 for EMEP. By contrast, the OMI+MODIS DA reduced sulfate biases against CASTNET and EMEP to 0.13–0.72 μg m^{-3} (11–129%). These bias reductions were generally smaller than those from TROPOMI+VIIRS DA. It also produced larger negative and positive biases against EANET and ATom-4 than those in the CTL run, respectively. RMSEs for OMI+MODIS DA were comparable to or 16–29% larger than those from TROPOMI+VIIRS DA for ATom-4, CASTNET, and EMEP, although the RMSE relative to EANET was 2% smaller.

The negative model biases and RMSEs for nitrate aerosols compared with independent observations ranged from 0.005 to 0.43 μg m^{-3} ($-$18–75%) and from 0.08 to 0.58 μg m^{-3} (99–266%), respectively, with correlation coefficients of 0.004–0.59. With the TROPOMI+VIIRS DA, negative biases against EMEP, CASTNET, and EANET were reduced to 0.06–0.23 μg m^{-3} ($-$15–40%), while the negative bias against ATom-4 slightly increased. RMSEs relative to ATom-4, CASTNET, and EANET were decreased by 3–27%, whereas correlation coefficients against most networks (except EANET) were degraded. The OMI+MODIS DA reduced negative biases against EMEP, CASTNET, and EANET to 0.05–0.28 μg m^{-3} ($-$12–49%). These reductions were larger than those from TROPOMI+VIIRS DA for EMEP and CASTNET but smaller for EANET. However, the positive bias against ATom-4 increased more strongly in OMI+MODIS DA than in TROPOMI+VIIRS DA. RMSEs in OMI+MODIS DA were comparable to or 3–9% larger than those in TROPOMI+VIIRS DA for CASTNET, EMEP, and EANET, but 29% smaller for ATom-4.

The model biases for ammonium aerosols compared with EMEP, EANET, and ATom-4 were negative by up to ˇ0.13 μg m^{-3} (by up to $-$25%), whereas the bias against CASTNET was slightly positive by 0.005 μg m^{-3} (by 1.3%). The RMSEs ranged from 0.15 to 0.34 μg m^{-3} (39–202%), with correlation coefficients of 0.32–0.60. In many cases, TROPOMI+VIIRS DA increased the biases and RMSEs for ammonium by factors of up to 6.5. Biases against EMEP and CASTNET increased by up to a factor of 6.6 in the OMI+MODIS DA.

The negative model biases and RMSEs for $PM_{2.5}$ total mass concentrations ranged from 1.7 to 2.2 μg m^{-3} (18–50%) and from 2.5 to 4.2 μg m^{-3} (34–172%), respectively, with correlation coefficients of 0.09–0.65. With the TROPOMI+VIIRS DA, negative biases against AQS, EEA AQ e-reporting, and Japanese and AirKorea networks were reduced to 0.6–1.5 μg m^{-3} ($-$5–33%). RMSEs decreased by 4–12% for AQS and EEA but increased by 9% for Japanese and AirKorea networks, while correlation coefficients against AQS were improved slightly. In the OMI+MODIS DA, negative biases were reduced to 1.0–1.1 μg m^{-3} ($-$24–25%) for AQS and EEA and were nearly eliminated for Japanese and AirKorea networks, representing reductions comparable to or larger than those from TROPOMI+VIIRS DA. RMSEs were 0.3–8% larger than those in TROPOMI+VIIRS DA for AQS and EEA, but 11% smaller for the Japanese and AirKorea networks.

Overall the results suggest benefits of assimilating current generation satellite constellations for constraining secondary inorganic aerosols and AOD, though improvements for $PM_{2.5}$ were not consistently observed across all networks. This contrast can be attributed that trace gas retrieval uncertainties in TROPOMI which were much improved compared to OMI, while the AOD products were consistent between MODIS and VIIRS sensors for long-term satellite records for most regions, except for South Africa, India, and arid regions.

https://doi.org/10.5194/egusphere-2026-1681
Preprint. Discussion started: 27 April 2026

6 Discussion and conclusion

6.1 Summary

Despite the increasing sophistication of aerosol DA approaches, the impacts of integrating satellite observations of aerosols and their precursor gases on aerosol composition have not previously been evaluated in a fully coupled framework. In this study, we developed one of the most comprehensive approaches, simultaneously optimizing aerosol concentrations, primary aerosol emissions, and precursor gas emissions. By assimilating satellite observations of AOD and trace gases within a DA framework, we improved estimates of the global distribution and chemical composition of aerosols.

The simultaneous assimilation of AOD and trace gas observations improved agreement with independent aircraft and surface in-situ observations compared with conventional approaches that assimilate AOD or trace gases separately. Improvements in sulfate and ammonium aerosols ranged 18–98% relative to AOD-only assimilation and 63–97% relative to trace-gas-only DA in many regions, except for Europe. Furthermore, agreements with $PM_{2.5}$ observations over East Asia improved by 56% compared with the conventional AOD-only DA. The assimilation of trace gases primarily drove corrections to SNA aerosols through adjustments in precursor emissions, while AOD assimilation constrained total $PM_{2.5}$ mass and benefited from the improved aerosol composition balance provided by trace gas assimilation.

The optimized emissions show substantial adjustments relative to *a prior* emission inventories. Global SO_2 and soil dust emissions decreased to 29.6 Tg S yr^{-1} and 1257.9 Tg yr^{-1} (reductions of 30% and 60%), whereas global NO_x and carbonaceous aerosol emissions increased to 63.6 Tg N yr^{-1} and 103.3 Tg C yr^{-1} (increases of 30% and 15%). These emission adjustments were primarily driven by trace-gas observations for SO_2 and NO_x, and by AOD observations for carbonaceous aerosols and dust emissions.

6.2 Forecast model performance

The performance of data assimilation is influenced by uncertainties in the forecast model, particularly associated with aerosols and their precursors. For example, the relationship between aerosol mass concentrations and AOD depends on aerosol optical parameters (e.g., mass extinction coefficient and single scattering albedo), which are strongly influenced by aerosol microphysical properties. Consequently, incorporating explicit aerosol microphysics (e.g., Yu et al., 2012; Tilmes et al., 2023) or simplified parameterizations (Zhai et al., 2021) into the forecast model could improve the model performance in simulating AOD. The lack of super-coarse dust in the forecast model in this study likely contributes an underestimation of the top-down dust emission estimates (Kok et al., 2021).

Furthermore, uncertainties in the model deposition and chemical reaction processes of aerosol precursors, such as NH_3, HNO_3, and SO_2, can influence the estimates of precursor emissions, aerosol formation, and aerosol composition. The pH dependency of dry deposition processes at wet surfaces can increases the NH_3 and SO_2 concentrations (Luo et al., 2019, 2020). The forecast model used in this study showed positive model biases in NH_3 relative to the CrIS satellite retrievals over the eastern United States, Europe, eastern China, northern India, and Central Africa (Fig. S1), which in turn contributed to positive biases in nitrate aerosols. Although the forecast model does not include explicit representations of the NH_3 volatilization

https://doi.org/10.5194/egusphere-2026-1681
Preprint. Discussion started: 27 April 2026

processes over land, implementing these processes could improve the model performance for simulating NH_3 (Zhu et al., 2015; Cao et al., 2022). Such model developments will be necessary to enhance the data assimilation performance in future studies.

6.3 Additional observational constraints

Additional constraints from emerging satellite instruments and products are expected to provide more comprehensive information for aerosol data assimilation, particularly with respect to vertical structure and speciation. For example, vertical aerosol extinction profiles from CALIOP (Winker et al., 2013) offer valuable information on aerosol layer heights. In addition, multi-wavelength AOD and absorbing AOD observations, such as those from POLDER/PARASOL (Tanré et al., 2011), are anticipated to help constrain aerosol microphysical properties and composition (Li et al., 2022b; Tsikerdekis et al., 2023). Advanced retrievals of single scattering albedo (SSA) and Ångström exponent (AE) as well as AOD derived from PACE/SPEXone (Fu et al., 2025), MetOp-SG-A/3MI (Fougnie et al., 2018), and CO2M/MAP (Lu et al., 2022) and vertical distributions from EarthCARE/ATLID (van Zadelhoff et al., 2023) should further improve constraints on aerosol properties. More detailed products, such as speciated PM retrievals from the PLANTiNO-2/MAIA instrument (Diner et al., 2018), are also expected to provide additional constraints on aerosol composition over selected target areas and their subsequent outflows. The combined use of diverse satellite datasets introduces new technical challenges, including inter-instrument biases and inconsistencies among retrieval products. Bias correction across multiple observing systems, as implemented in the MERRA-2 reanalysis (Randles et al., 2017), will be essential for improving the consistency and accuracy of aerosol analyses.

Ammonium aerosols remained unconstrained directly in the present framework. Optimizing NH_3 emissions using satellite retrievals such as CrIS (Shephard and Cady-Pereira, 2015) is expected to improve the representation of nitrate and ammonium aerosol formation through aerosol chemistry and thermodynamic equilibrium (Dang et al., 2024). Comparison with CrIS observations (Fig. S1) indicates that the model overestimates surface NH_3 over Europe, the eastern United States, China, northern India, and central Africa, while underestimating it over the central United States, South America, North Africa, and West Asia. To assess the potential impact of NH_3 assimilation under the current model configuration, we conducted a sensitivity experiment in which NH_3 emissions were adjusted based on the ratio of surface NH_3 concentrations derived from satellite retrievals to those from model forecast without applying data assimilation. This adjustment partially reduced the remaining nitrate aerosol biases relative to EMEP and CASTNET observations by 0.2 and 0.04 $\mu g\ m^{-3}$, respectively (Fig. S2). Nevertheless, important challenges remain, because the forecast models that do not include a bidirectional flux scheme can introduce substantial biases in inferred NH_3 emissions (Marais et al., 2021). Future studies that incorporate NH_3 observations into the existing assimilation framework, as similarly tested by Henze et al. (2009), together with improvements in model process representation, are expected to further enhance aerosol analyses.

Another important component is volatile organic compound (VOC) emissions, which are key precursors of secondary organic aerosol formation. They constitute a major fraction of aerosol mass in developed regions (Attwood et al., 2014). However, the present DA system does not yet optimize VOC emissions. Assimilation of satellite retrievals of formaldehyde (De Smedt et al.,

https://doi.org/10.5194/egusphere-2026-1681
Preprint. Discussion started: 27 April 2026

2018), glyoxal (Lerot et al., 2021), and isoprene (Wells et al., 2022) offers considerable potential to improve the representation of global VOC distributions, aerosol formation, and aerosol composition.

While trace gas DA updates precursor emissions and thereby modifies aerosol speciation during the forecast step, the current AOD DA retains the modeled aerosol composition balance during the analysis step. Incorporating cross-variable background error covariances between an expanded set of state variables, including aerosol optical properties (AOD, SSA, and AE) and individual aerosol components, would improve the DA system's ability to exploit observational information by propagating it across a broader state vector. Nevertheless, achieving these improvements requires accurate error covariance estimates. Important technical challenges remain, including the detailed representation of aerosol chemistry in the forecast model and the reduction of sampling error through larger ensemble sizes.

6.4 Climate and health applications

Aerosols and their precursor emissions remain a major source of uncertainty in climate impact assessments, including those in CMIP6 (Wang et al., 2021). Because different aerosol components have distinct climatic effects (Li et al., 2022a), their evaluation is important, yet still limited by sparse observational coverage. Likewise, mortality risks associated with $PM_{2.5}$ exposure can be estimated more accurately when chemical composition is considered, rather than using only total PM2.5 mass as in many previous studies (Beelen et al., 2015; Ueda et al., 2016; Thurston et al., 2016; Weichenthal et al., 2024; Crouse et al., 2016; Xue et al., 2021). Long-term reanalysis datasets based on the simultaneous assimilation of aerosol and trace-gas observations can provide observationally constrained aerosol speciation information to address these limitations.

6.5 Conclusion

Overall, our results demonstrate that the simultaneous assimilation of satellite AOD and trace gas observations provides clear advantages for improving aerosol composition estimates. These advances have been enabled by the expansion of satellite observing systems and by improvements in sensor capabilities. For example, the use of TROPOMI and VIIRS observations produced more accurate analyses than earlier-generation datasets such as OMI and MODIS. Unlike conventional approaches that do not explicitly optimize aerosol composition balance, the framework presented here provides observationally constrained long-term aerosol reanalysis datasets that are highly valuable for climate studies and for assessments of human health impacts. Future improvements could be achieved by assimilating additional observations, including multiwavelength AOD, NH_3, and NMVOCs, as well as high-temporal-resolution measurements from geostationary satellite platforms.

Code availability. The source code is not publicly available because of license restriction. The source code is available from Kengo Sudo (kengo@nagoya-u.jp) upon request. The source code for the data assimilation system is available from Kazuyuki Miyazaki (Kazuyuki.Miyazaki@jpl.nasa.gov) upon request.

https://doi.org/10.5194/egusphere-2026-1681
Preprint. Discussion started: 27 April 2026

Data availability. The data assimilation results are available online (https://doi.org/10.6084/m9.figshare.31848628). The TROPOMI and OMI NO2 satellite retrievals are publicly available at the TEMIS website (https://www.temis.nl/airpollution/no2col/no2regio_tropomi.php, last access: August 20, 2024). The TROPOMI SO2 retrievals were obtained from the S5P-PAL data portal (https://data-portal.s5p-pal.com/browser; last access: September 1, 2024). MLS ozone, HNO_3, MOPITT CO, MODIS AOD, VIIRS AOD from the NASA Aura, EOS Terra, Aqua, NOAA Suomi-NPP, and NOAA-20 satellites are available at the NASA's EARTHDATA (https://earthdata.nasa.gov/, last access: May 10, 2025). Surface PM2.5 measurement data were downloaded from EEA (https://www.eea.europa.eu/), US EPA (https://www.epa.gov/aqs), NIES (http://www.nies.go.jp/), and Air Korea (https://airkorea.or.kr/web/). Sulfate, nirtate, and ammonium aerosol data were obtained from EMEP (http://ebas.nilu.no/), CASTNET (https://www.epa.gov/castnet), and EANET (http://www.eanet.asia/). NASA's aircraft-campaign observation data are available at NASA Langley Researce Center website (https://www-air.larc.nasa.gov/missions/korus-aq/) for KORUS-AQ and at Oak Ridge National Laboratory website (https://daac.ornl.gov/ATOM/campaign/) for ATom-4.

Author contributions. T.S. and K.M. designed the research; T.S. conducted the model and data assimilation calculations, and performed the analysis; H.E. and P.R. curated S5P/TROPOMI retrievals and applied the super-observation approach to them; All the authors have contributed to the research, drafting of paper text, and approved the final version of the manuscript.

Competing interests. One of the co-authors is a member of the editorial board of Atmospheric Chemistry and Physics. The authors have no other competing interests to declare.

Acknowledgements. This study was supported by the Environmental Restoration and Conservation Agency (Grant nos. JPMEERF20222001 and JPMEERF20252001), and the Japan Society for the Promotion of Science (Grant nos. 22K12353, 23H04971, and 25K00377). Part of this work was conducted at the Jet Propulsion Laboratory, California Institute of Technology, under contract with NASA. Authors thank Dr. Jaehwa Lee and Dr. Andrew Sayer for advice on the use of the VIIRS DB version 2 product. The model and data assimilation calculations were conducted using the Earth Simulator with the support of the Japan Agency for Marine-Earth Science and Technology.

https://doi.org/10.5194/egusphere-2026-1681
Preprint. Discussion started: 27 April 2026

References

Attwood, A. R., Washenfelder, R. A., Brock, C. A., Hu, W., Baumann, K., Campuzano-Jost, P., Day, D. A., Edgerton, E. S., Murphy, D. M., Palm, B. B., McComiskey, A., Wagner, N. L., de Sá, S. S., Ortega, A., Martin, S. T., Jimenez, J. L., and Brown, S. S.: Trends in sulfate and organic aerosol mass in the Southeast U.S.: Impact on aerosol optical depth and radiative forcing, Geophys. Res. Lett., 41, 7701–7709, https://doi.org/https://doi.org/10.1002/2014GL061669, 2014.

Bahreini, R., Ervens, B., Middlebrook, A. M., Warneke, C., de Gouw, J. A., DeCarlo, P. F., Jimenez, J. L., Brock, C. A., Neuman, J. A., Ryerson, T. B., Stark, H., Atlas, E., Brioude, J., Fried, A., Holloway, J. S., Peischl, J., Richter, D., Walega, J., Weibring, P., Wollny, A. G., and Fehsenfeld, F. C.: Organic aerosol formation in urban and industrial plumes near Houston and Dallas, Texas, J. Geophys. Res., 114, https://doi.org/10.1029/2008JD011493, 2009.

Barnes, W., Pagano, T., and Salomonson, V.: Prelaunch characteristics of the Moderate Resolution Imaging Spectroradiometer (MODIS) on EOS-AM1, IEEE Transactions on Geoscience and Remote Sensing, 36, 1088–1100, https://doi.org/10.1109/36.700993, 1998.

Beelen, R., Hoek, G., Raaschou-Nielsen, O., Stafoggia, M., Andersen, Z. J., Weinmayr, G., Hoffmann, B., Wolf, K., Samoli, E., Fischer, P. H., Nieuwenhuijsen, M. J., Xun, W. W., Katsouyanni, K., Dimakopoulou, K., Marcon, A., Vartiainen, E., Lanki, T., Yli-Tuomi, T., Oftedal, B., Schwarze, P. E., Nafstad, P., Faire, U. D., Pedersen, N. L., Östenson, C.-G., Fratiglioni, L., Penell, J., Korek, M., Pershagen, G., Eriksen, K. T., Overvad, K., Sørensen, M., Eeftens, M., Peeters, P. H., Meliefste, K., Wang, M., de Mesquita, H. B. B., Sugiri, D., Krämer, U., Heinrich, J., de Hoogh, K., Key, T., Peters, A., Hampel, R., Concin, H., Nagel, G., Jaensch, A., Ineichen, A., Tsai, M.-Y., Schaffner, E., Probst-Hensch, N. M., Schindler, C., Ragettli, M. S., Vilier, A., Clavel-Chapelon, F., Declercq, C., Ricceri, F., Sacerdote, C., Galassi, C., Migliore, E., Ranzi, A., Cesaroni, G., Badaloni, C., Forastiere, F., Katsoulis, M., Trichopoulou, A., Keuken, M., Jedynska, A., Kooter, I. M., Kukkonen, J., Sokhi, R. S., Vineis, P., and Brunekreef, B.: Natural-Cause Mortality and Long-Term Exposure to Particle Components: An Analysis of 19 European Cohorts within the Multi-Center ESCAPE Project, Environ. Health Perspect., 123, 525–533, https://doi.org/10.1289/ehp.1408095, 2015.

Benedetti, A., Morcrette, J.-J., Boucher, O., Dethof, A., Engelen, R. J., Fisher, M., Flentje, H., Huneeus, N., Jones, L., Kaiser, J. W., Kinne, S., Mangold, A., Razinger, M., Simmons, A. J., and Suttie, M.: Aerosol analysis and forecast in the European Centre for Medium-Range Weather Forecasts Integrated Forecast System: 2. Data assimilation, J. Geophys. Res., 114, https://doi.org/10.1029/2008JD011115, 2009.

Boersma, K. F., Eskes, H., Richter, A., De Smedt, I., Lorente, A., Beirle, S., Van Geffen, J., Peters, E., Van Roozendael, M., and Wagner, T.: QA4ECV NO2 tropospheric and stratospheric vertical column data from OMI (Version 1.1) [Data set], https://doi.org/10.21944/qa4ecv-no2-omi-v1.1, 2017.

Boersma, K. F., Eskes, H. J., Richter, A., De Smedt, I., Lorente, A., Beirle, S., van Geffen, J. H. G. M., Zara, M., Peters, E., Van Roozendael, M., Wagner, T., Maasakkers, J. D., van der A, R. J., Nightingale, J., De Rudder, A., Irie, H., Pinardi, G., Lambert, J.-C., and Compernolle, S. C.: Improving algorithms and uncertainty estimates for satellite NO_2 retrievals: results from the quality assurance for the essential climate variables (QA4ECV) project, Atmos. Meas. Tech., 11, 6651–6678, https://doi.org/10.5194/amt-11-6651-2018, 2018.

Burnett, R., Chen, H., Szyszkowicz, M., Fann, N., Hubbell, B., Pope, C. A., Apte, J. S., Brauer, M., Cohen, A., Weichenthal, S., Coggins, J., Di, Q., Brunekreef, B., Frostad, J., Lim, S. S., Kan, H., Walker, K. D., Thurston, G. D., Hayes, R. B., Lim, C. C., Turner, M. C., Jerrett, M., Krewski, D., Gapstur, S. M., Diver, W. R., Ostro, B., Goldberg, D., Crouse, D. L., Martin, R. V., Peters, P., Pinault, L., Tjepkema, M., van Donkelaar, A., Villeneuve, P. J., Miller, A. B., Yin, P., Zhou, M., Wang, L., Janssen, N. A. H., Marra, M., Atkinson, R. W., Tsang, H., Thach, T. Q., Cannon, J. B., Allen, R. T., Hart, J. E., Laden, F., Cesaroni, G., Forastiere, F., Weinmayr, G., Jaensch, A., Nagel, G., Concin,

https://doi.org/10.5194/egusphere-2026-1681
Preprint. Discussion started: 27 April 2026

H., and Spadaro, J. V.: Global estimates of mortality associated with long-term exposure to outdoor fine particulate matter, Proc. Natl. Acad. Sci., 115, 9592–9597, https://doi.org/10.1073/pnas.1803222115, 2018.

Cao, C., Xiong, J., Blonski, S., Liu, Q., Uprety, S., Shao, X., Bai, Y., and Weng, F.: Suomi NPP VIIRS sensor data record verification, validation, and long-term performance monitoring, J. Geophys. Res., 118, 11,664–11,678, https://doi.org/10.1002/2013JD020418, 2013.

Cao, H., Henze, D. K., Zhu, L., Shephard, M. W., Cady-Pereira, K., Dammers, E., Sitwell, M., Heath, N., Lonsdale, C., Bash, J. O., Miyazaki, K., Flechard, C., Fauvel, Y., Kruit, R. W., Feigenspan, S., Brümmer, C., Schrader, F., Twigg, M. M., Leeson, S., Tang, Y. S., Stephens, A. C. M., Braban, C., Vincent, K., Meier, M., Seitler, E., Geels, C., Ellermann, T., Sanocka, A., and Capps, S. L.: 4D-Var Inversion of European NH3 Emissions Using CrIS NH3 Measurements and GEOS-Chem Adjoint With Bi-Directional and Uni-Directional Flux Schemes, J. Geophys. Res., 127, e2021JD035 687, https://doi.org/10.1029/2021JD035687, 2022.

Chen, C., Dubovik, O., Henze, D. K., Chin, M., Lapyonok, T., Schuster, G. L., Ducos, F., Fuertes, D., Litvinov, P., Li, L., Lopatin, A., Hu, Q., and Torres, B.: Constraining global aerosol emissions using POLDER/PARASOL satellite remote sensing observations, Atmos. Chem. Phys., 19, 14 585–14 606, https://doi.org/10.5194/acp-19-14585-2019, 2019.

Chen, C., Dubovik, O., Schuster, G. L., Chin, M., Henze, D. K., Lapyonok, T., Li, Z., Derimian, Y., and Zhang, Y.: Multi-angular polarimetric remote sensing to pinpoint global aerosol absorption and direct radiative forcing, Nat. Comm., 13, 7459, https://doi.org/10.1038/s41467-022-35147-y, 2022.

Chen, J. and Hoek, G.: Long-term exposure to PM and all-cause and cause-specific mortality: A systematic review and meta-analysis., Environ. Int., 143, 105 974, https://doi.org/10.1016/j.envint.2020.105974, 2020.

Chen, Y., Hall, J., van Wees, D., Andela, N., Hantson, S., Giglio, L., van der Werf, G. R., Morton, D. C., and Randerson, J. T.: Multi-decadal trends and variability in burned area from the fifth version of the Global Fire Emissions Database (GFED5), Earth Syst. Sci. Data, 15, 5227–5259, https://doi.org/10.5194/essd-15-5227-2023, 2023.

Chow, J. C., Watson, J. G., Lowenthal, D. H., Chen, L. W. A., Tropp, R. J., Park, K., and Magliano, K. A.: PM2.5 and PM10 Mass Measurements in California's San Joaquin Valley, Aerosol Sci. Technol., 40, 796–810, https://doi.org/10.1080/02786820600623711, 2006.

Cohen, A. J., Brauer, M., Burnett, R., Anderson, H. R., Frostad, J., Estep, K., Balakrishnan, K., Brunekreef, B., Dandona, L., Dandona, R., Feigin, V., Freedman, G., Hubbell, B., Jobling, A., Kan, H., Knibbs, L., Liu, Y., Martin, R., Morawska, L., Pope, C Arden, I., Shin, H., Straif, K., Shaddick, G., Thomas, M., van Dingenen, R., van Donkelaar, A., Vos, T., Murray, C. J. L., and Forouzanfar, M. H.: Estimates and 25-year trends of the global burden of disease attributable to ambient air pollution: an analysis of data from the Global Burden of Diseases Study 2015, The Lancet, 389, 1907–1918, https://doi.org/10.1016/S0140-6736(17)30505-6, 2017.

Copernicus Sentinel-5P (processed by ESA): TROPOMI Level 2 Nitrogen Dioxide total column products. Version 02., https://doi.org/10.5270/S5P-9bnp8q8, 2021.

Crawford, J. H., Ahn, J.-Y., Al-Saadi, J., Chang, L., Emmons, L. K., Kim, J., Lee, G., Park, J.-H., Park, R. J., Woo, J. H., Song, C.-K., Hong, J.-H., Hong, Y.-D., Lefer, B. L., Lee, M., Lee, T., Kim, S., Min, K.-E., Yum, S. S., Shin, H. J., Kim, Y.-W., Choi, J.-S., Park, J.-S., Szykman, J. J., Long, R. W., Jordan, C. E., Simpson, I. J., Fried, A., Dibb, J. E., Cho, S., and Kim, Y. P.: The Korea–United States Air Quality (KORUS-AQ) field study, Elem. Sci. Anth., 9, 00 163, https://doi.org/10.1525/elementa.2020.00163, 2021.

Crippa, M., Guizzardi, D., Pagani, F., Schiavina, M., Melchiorri, M., Pisoni, E., Graziosi, F., Muntean, M., Maes, J., Dijkstra, L., Van Damme, M., Clarisse, L., and Coheur, P.: Insights into the spatial distribution of global, national, and subnational greenhouse gas emissions in the Emissions Database for Global Atmospheric Research (EDGAR v8.0), Earth Syst. Sci. Data, 16, 2811–2830, https://doi.org/10.5194/essd-16-2811-2024, 2024.

https://doi.org/10.5194/egusphere-2026-1681
Preprint. Discussion started: 27 April 2026

Crounse, J. D., McKinney, K. A., Kwan, A. J., and Wennberg, P. O.: Measurement of Gas-Phase Hydroperoxides by Chemical Ionization Mass Spectrometry, Anal. Chem., 78, 6726–6732, https://doi.org/10.1021/ac0604235, 2006.

Crouse, D. L., Philip, S., van Donkelaar, A., Martin, R. V., Jessiman, B., Peters, P. A., Weichenthal, S., Brook, J. R., Hubbell, B., and Burnett, R. T.: A New Method to Jointly Estimate the Mortality Risk of Long-Term Exposure to Fine Particulate Matter and its Components, Sci. Rep., 6, 18 916, https://doi.org/10.1038/srep18916, 2016.

Dang, R., Jacob, D. J., Zhai, S., Yang, L. H., Pendergrass, D. C., Coheur, P., Clarisse, L., Van Damme, M., Choi, J.-s., Park, J.-s., Liu, Z., Xie, P., and Liao, H.: A Satellite-Based Indicator for Diagnosing Particulate Nitrate Sensitivity to Precursor Emissions: Application to East Asia, Europe, and North America, Environ. Sci. Tech., 58, 20 101–20 113, https://doi.org/10.1021/acs.est.4c08082, 2024.

De Smedt, I., Theys, N., Yu, H., Danckaert, T., Lerot, C., Compernolle, S., Van Roozendael, M., Richter, A., Hilboll, A., Peters, E., Pedergnana, M., Loyola, D., Beirle, S., Wagner, T., Eskes, H., van Geffen, J., Boersma, K. F., and Veefkind, P.: Algorithm theoretical baseline for formaldehyde retrievals from S5P TROPOMI and from the QA4ECV project, Atmos. Meas. Tech., 11, 2395–2426, https://doi.org/10.5194/amt-11-2395-2018, 2018.

DeCarlo, P. F., Kimmel, J. R., Trimborn, A., Northway, M. J., Jayne, J. T., Aiken, A. C., Gonin, M., Fuhrer, K., Horvath, T., Docherty, K. S., Worsnop, D. R., and Jimenez, J. L.: Field-Deployable, High-Resolution, Time-of-Flight Aerosol Mass Spectrometer, Anal. Chem., 78, 8281–8289, https://doi.org/10.1021/ac061249n, 2006.

Dee, D. P. and Da Silva, A. M.: Data assimilation in the presence of forecast bias, Q. J. R. Meteor. Soc., 124, 269–295, https://doi.org/10.1002/qj.49712454512, 1998.

Deeter, M. N., Edwards, D. P., Francis, G. L., Gille, J. C., Martínez-Alonso, S., Worden, H. M., and Sweeney, C.: A climate-scale satellite record for carbon monoxide: the MOPITT Version 7 product, Atmos. Meas. Tech., 10, 2533–2555, https://doi.org/10.5194/amt-10-2533-2017, 2017.

Diner, D. J., Boland, S. W., Brauer, M., Bruegge, C., Burke, K. A., Chipman, R., Girolamo, L. D., Garay, M. J., Hasheminassab, S., Hyer, E., Jerrett, M., Jovanovic, V., Kalashnikova, O. V., Liu, Y., Lyapustin, A. I., Martin, R. V., Nastan, A., Ostro, B. D., Ritz, B., Schwartz, J., Wang, J., and Xu, F.: Advances in multiangle satellite remote sensing of speciated airborne particulate matter and association with adverse health effects: from MISR to MAIA, J. Appl. Remote Sens., 12, 042 603, https://doi.org/10.1117/1.JRS.12.042603, 2018.

Ding, J., van der A, R., Eskes, H., Dammers, E., Shephard, M., Wichink Kruit, R., Guevara, M., and Tarrason, L.: Ammonia emission estimates using CrIS satellite observations over Europe, Atmos. Chem. Phys., 24, 10 583–10 599, https://doi.org/10.5194/acp-24-10583-2024, 2024.

Eskes, H. J. and Boersma, K. F.: Averaging kernels for DOAS total-column satellite retrievals, Atmos. Chem. Phys., 3, 1285–1291, https://doi.org/10.5194/acp-3-1285-2003, 2003.

Evensen, G.: The ensemble Kalman filter for combined state and parameter estimation, IEEE Control Syst., 29, 83–104, https://doi.org/10.1109/MCS.2009.932223, 2009.

Fairlie, T. D., Jacob, D. J., Dibb, J. E., Alexander, B., Avery, M. A., van Donkelaar, A., and Zhang, L.: Impact of mineral dust on nitrate, sulfate, and ozone in transpacific Asian pollution plumes, Atmos. Chem. Phys., 10, 3999–4012, https://doi.org/10.5194/acp-10-3999-2010, 2010.

Fioletov, V., McLinden, C. A., Kharol, S. K., Krotkov, N. A., Li, C., Joiner, J., Moran, M. D., Vet, R., Visschedijk, A. J. H., and Denier van der Gon, H. A. C.: Multi-source SO_2 emission retrievals and consistency of satellite and surface measurements with reported emissions, Atmos. Chem. Phys., 17, 12 597–12 616, https://doi.org/10.5194/acp-17-12597-2017, 2017.

https://doi.org/10.5194/egusphere-2026-1681
Preprint. Discussion started: 27 April 2026

Fioletov, V. E., McLinden, C. A., Krotkov, N., Li, C., Joiner, J., Theys, N., Carn, S., and Moran, M. D.: A global catalogue of large SO_2 sources and emissions derived from the Ozone Monitoring Instrument, Atmos. Chem. Phys., 16, 11 497–11 519, https://doi.org/10.5194/acp-16-11497-2016, 2016.

Fougnie, N., Marbach, T., Lacan, A., Lang, R., Schlüssel, P., Poli, G., Munro, R., and Couto, A. B.: The multi-viewing multi-channel multi-polarisation imager – Overview of the 3MI polarimetric mission for aerosol and cloud characterization, J. Quant. Spectrosc. Radiat. Transf., 219, 23–32, https://doi.org/https://doi.org/10.1016/j.jqsrt.2018.07.008, 2018.

Fu, G., Hasekamp, O., Rietjens, J., Smit, M., Di Noia, A., Cairns, B., Wasilewski, A., Diner, D., Seidel, F., Xu, F., Knobelspiesse, K., Gao, M., da Silva, A., Burton, S., Hostetler, C., Hair, J., and Ferrare, R.: Aerosol retrievals from different polarimeters during the ACEPOL campaign using a common retrieval algorithm, Atmos. Meas. Tech., 13, 553–573, https://doi.org/10.5194/amt-13-553-2020, 2020.

Fu, G., Rietjens, J., Laasner, R., van der Schaaf, L., van Hees, R., Yuan, Z., van Diedenhoven, B., Hannadige, N., Landgraf, J., Smit, M., Knobelspiesse, K., Cairns, B., Gao, M., Franz, B., Werdell, J., and Hasekamp, O.: Aerosol Retrievals From SPEXone on the NASA PACE Mission: First Results and Validation, Geophys. Res. Lett., 52, https://doi.org/https://doi.org/10.1029/2024GL113525, 2025.

Garay, M. J., Witek, M. L., Kahn, R. A., Seidel, F. C., Limbacher, J. A., Bull, M. A., Diner, D. J., Hansen, E. G., Kalashnikova, O. V., Lee, H., Nastan, A. M., and Yu, Y.: Introducing the 4.4 km spatial resolution Multi-Angle Imaging SpectroRadiometer (MISR) aerosol product, Atmos. Meas. Tech., 13, 593–628, https://doi.org/10.5194/amt-13-593-2020, 2020.

Garrigues, S., Remy, S., Chimot, J., Ades, M., Inness, A., Flemming, J., Kipling, Z., Laszlo, I., Benedetti, A., Ribas, R., Jafariserajehlou, S., Fougnie, B., Kondragunta, S., Engelen, R., Peuch, V.-H., Parrington, M., Bousserez, N., Vazquez Navarro, M., and Agusti-Panareda, A.: Monitoring multiple satellite aerosol optical depth (AOD) products within the Copernicus Atmosphere Monitoring Service (CAMS) data assimilation system, Atmos. Chem. Phys., 22, 14 657–14 692, https://doi.org/10.5194/acp-22-14657-2022, 2022.

Ginoux, P., Prospero, J. M., Gill, T. E., Hsu, N. C., and Zhao, M.: Global-scale attribution of anthropogenic and natural dust sources and their emission rates based on MODIS Deep Blue aerosol products, Rev. Geophys., 50, https://doi.org/10.1029/2012RG000388, 2012.

Gliß, J., Mortier, A., Schulz, M., Andrews, E., Balkanski, Y., Bauer, S. E., Benedictow, A. M. K., Bian, H., Checa-Garcia, R., Chin, M., Ginoux, P., Griesfeller, J. J., Heckel, A., Kipling, Z., Kirkevåg, A., Kokkola, H., Laj, P., Le Sager, P., Lund, M. T., Lund Myhre, C., Matsui, H., Myhre, G., Neubauer, D., van Noije, T., North, P., Olivié, D. J. L., Rémy, S., Sogacheva, L., Takemura, T., Tsigaridis, K., and Tsyro, S. G.: AeroCom phase III multi-model evaluation of the aerosol life cycle and optical properties using ground- and space-based remote sensing as well as surface in situ observations, Atmos. Chem. Phys., 21, 87–128, https://doi.org/10.5194/acp-21-87-2021, 2021.

Guizzardi, D., Crippa, M., Butler, T., Keating, T., Wu, R., Kaminski, J., Kuenen, J., Kurokawa, J., Chatani, S., Morikawa, T., Pouliot, G., Racine, J., Moran, M. D., Klimont, Z., Manseau, P. M., Mashayekhi, R., Henderson, B. H., Smith, S. J., Hoesly, R., Muntean, M., Banja, M., Schaaf, E., Pagani, F., Woo, J.-H., Kim, J., Pisoni, E., Zhang, J., Niemi, D., Sassi, M., Duhamel, A., Ansari, T., Foley, K., Geng, G., Chen, Y., and Zhang, Q.: The HTAP_v3.2 emission mosaic: merging regional and global monthly emissions (2000–2020) to support air quality modelling and policies, Earth Syst. Sci. Data, 17, 5915–5950, https://doi.org/10.5194/essd-17-5915-2025, 2025.

Hardacre, C., Mulcahy, J. P., Pope, R. J., Jones, C. G., Rumbold, S. T., Li, C., Johnson, C., and Turnock, S. T.: Evaluation of SO_2, SO_4^{2-} and an updated SO_2 dry deposition parameterization in the United Kingdom Earth System Model, Atmos. Chem. Phys., 21, 18 465–18 497, https://doi.org/10.5194/acp-21-18465-2021, 2021.

Henze, D. K., Seinfeld, J. H., and Shindell, D. T.: Inverse modeling and mapping US air quality influences of inorganic $PM_{2.5}$ precursor emissions using the adjoint of GEOS-Chem, Atmos. Chem. Phys., 9, 5877–5903, https://doi.org/10.5194/acp-9-5877-2009, 2009.

Hersbach, H., Bell, B., Berrisford, P., Hirahara, S., Horányi, A., Muñoz-Sabater, J., Nicolas, J., Peubey, C., Radu, R., Schepers, D., Simmons, A., Soci, C., Abdalla, S., Abellan, X., Balsamo, G., Bechtold, P., Biavati, G., Bidlot, J., Bonavita, M., De Chiara, G., Dahlgren, P., Dee,

https://doi.org/10.5194/egusphere-2026-1681
Preprint. Discussion started: 27 April 2026

D., Diamantakis, M., Dragani, R., Flemming, J., Forbes, R., Fuentes, M., Geer, A., Haimberger, L., Healy, S., Hogan, R. J., Hólm, E., Janisková, M., Keeley, S., Laloyaux, P., Lopez, P., Lupu, C., Radnoti, G., de Rosnay, P., Rozum, I., Vamborg, F., Villaume, S., and Thépaut, J.-N.: The ERA5 global reanalysis, Q. J. R. Meteor. Soc., 146, 1999–2049, https://doi.org/https://doi.org/10.1002/qj.3803, 2020.

Hobbs, P. V., Reid, J. S., Kotchenruther, R. A., Ferek, R. J., and Weiss, R.: Direct Radiative Forcing by Smoke from Biomass Burning, Science, 275, 1777–1778, https://doi.org/10.1126/science.275.5307.1777, 1997.

Hoesly, R. M., Smith, S. J., Feng, L., Klimont, Z., Janssens-Maenhout, G., Pitkanen, T., Seibert, J. J., Vu, L., Andres, R. J., Bolt, R. M., Bond, T. C., Dawidowski, L., Kholod, N., Kurokawa, J.-I., Li, M., Liu, L., Lu, Z., Moura, M. C. P., O'Rourke, P. R., and Zhang, Q.: Historical (1750–2014) anthropogenic emissions of reactive gases and aerosols from the Community Emissions Data System (CEDS), Geosci. Model Dev., 11, 369–408, https://doi.org/10.5194/gmd-11-369-2018, 2018.

Holben, B., Eck, T., Slutsker, I., Tanré, D., Buis, J., Setzer, A., Vermote, E., Reagan, J., Kaufman, Y., Nakajima, T., Lavenu, F., Jankowiak, I., and Smirnov, A.: AERONET—A Federated Instrument Network and Data Archive for Aerosol Characterization, Remote Sens. Environ., 66, 1–16, https://doi.org/10.1016/S0034-4257(98)00031-5, 1998.

Hsu, N. C., Lee, J., Sayer, A. M., Carletta, N., Chen, S.-H., Tucker, C. J., Holben, B. N., and Tsay, S.-C.: Retrieving near-global aerosol loading over land and ocean from AVHRR, J. Geophys. Res., 122, 9968–9989, https://doi.org/10.1002/2017JD026932, 2017.

Hsu, N. C., Lee, J., Sayer, A. M., Kim, W., Bettenhausen, C., and Tsay, S.-C.: VIIRS Deep Blue Aerosol Products Over Land: Extending the EOS Long-Term Aerosol Data Records, J. Geophys. Res., 124, 4026–4053, https://doi.org/10.1029/2018JD029688, 2019.

Hua, W., Lou, S., Huang, X., Xue, L., Ding, K., Wang, Z., and Ding, A.: Diagnosing uncertainties in global biomass burning emission inventories and their impact on modeled air pollutants, Atmos. Chem. Phys., 24, 6787–6807, https://doi.org/10.5194/acp-24-6787-2024, 2024.

Huneeus, N., Chevallier, F., and Boucher, O.: Estimating aerosol emissions by assimilating observed aerosol optical depth in a global aerosol model, Atmos. Chem. Phys., 12, 4585–4606, https://doi.org/10.5194/acp-12-4585-2012, 2012.

Huneeus, N., Boucher, O., and Chevallier, F.: Atmospheric inversion of SO_2 and primary aerosol emissions for the year 2010, Atmos. Chem. Phys., 13, 6555–6573, https://doi.org/10.5194/acp-13-6555-2013, 2013.

Hunt, B. R., Kostelich, E. J., and Szunyogh, I.: Efficient data assimilation for spatiotemporal chaos: A local ensemble transform Kalman filter, Physica D, 230, 112–126, https://doi.org/10.1016/j.physd.2006.11.008, 2007.

Hyer, E. J., Reid, J. S., and Zhang, J.: An over-land aerosol optical depth data set for data assimilation by filtering, correction, and aggregation of MODIS Collection 5 optical depth retrievals, Atmos. Meas. Tech., 4, 379–408, https://doi.org/10.5194/amt-4-379-2011, 2011.

IPCC: Climate Change 2021: The Physical Science Basis. Contribution of Working Group I to the Sixth Assessment Report of the Intergovernmental Panel on Climate Change, 2021.

Jin, J., Pang, M., Segers, A., Han, W., Fang, L., Li, B., Feng, H., Lin, H. X., and Liao, H.: Inverse modeling of the 2021 spring super dust storms in East Asia, Atmos. Chem. Phys., 22, 6393–6410, https://doi.org/10.5194/acp-22-6393-2022, 2022.

K-1 model developers: K-1 Coupled GCM (MIROC) Description, Tech. rep., Center for Climate System Research (Univ. of Tokyo), National Institute for Environmental Studies, and Frontier Research Center for Global Change, https://ccsr.aori.u-tokyo.ac.jp/~hasumi/miroc_description.pdf, last access: 29 January 2024, 2004.

Kang, J.-S., Kalnay, E., Liu, J., Fung, I., Miyoshi, T., and Ide, K.: "Variable localization" in an ensemble Kalman filter: Application to the carbon cycle data assimilation, J. Geophys. Res., 116, https://doi.org/10.1029/2010JD014673, 2011.

https://doi.org/10.5194/egusphere-2026-1681
Preprint. Discussion started: 27 April 2026

Kim, D., Chin, M., Schuster, G., Yu, H., Takemura, T., Tuccella, P., Ginoux, P., Liu, X., Shi, Y., Matsui, H., Tsigaridis, K., Bauer, S. E., Kok, J. F., and Schulz, M.: Where Dust Comes From: Global Assessment of Dust Source Attributions With AeroCom Models, J. Geophys. Res., 129, e2024JD041 377, https://doi.org/10.1029/2024JD041377, 2024.

Kim, H., Park, R. J., Kim, S., Brune, W. H., Diskin, G. S., Fried, A., Hall, S. R., Weinheimer, A. J., Wennberg, P., Wisthaler, A., Blake, D. R., and Ullmann, K.: Observed versus simulated OH reactivity during KORUS-AQ campaign: Implications for emission inventory and chemical environment in East Asia, Elem. Sci. Anthro., 10, 00 030, https://doi.org/10.1525/elementa.2022.00030, 2022.

Kok, J. F., Adebiyi, A. A., Albani, S., Balkanski, Y., Checa-Garcia, R., Chin, M., Colarco, P. R., Hamilton, D. S., Huang, Y., Ito, A., Klose, M., Leung, D. M., Li, L., Mahowald, N. M., Miller, R. L., Obiso, V., Pérez García-Pando, C., Rocha-Lima, A., Wan, J. S., and Whicker, C. A.: Improved representation of the global dust cycle using observational constraints on dust properties and abundance, Atmos. Chem. Phys., 21, 8127–8167, https://doi.org/10.5194/acp-21-8127-2021, 2021.

Lee, C., Martin, R. V., van Donkelaar, A., Lee, H., Dickerson, R. R., Hains, J. C., Krotkov, N., Richter, A., Vinnikov, K., and Schwab, J. J.: SO2 emissions and lifetimes: Estimates from inverse modeling using in situ and global, space-based (SCIAMACHY and OMI) observations, J. Geophys. Res., 116, https://doi.org/https://doi.org/10.1029/2010JD014758, 2011.

Lee, J., Hsu, N. C., Kim, W. V., Sayer, A. M., and Tsay, S.-C.: VIIRS Version 2 Deep Blue Aerosol Products, J. Geophys. Res., 129, e2023JD040 082, https://doi.org/10.1029/2023JD040082, 2024.

Lerot, C., Hendrick, F., Van Roozendael, M., Alvarado, L. M. A., Richter, A., De Smedt, I., Theys, N., Vlietinck, J., Yu, H., Van Gent, J., Stavrakou, T., Müller, J.-F., Valks, P., Loyola, D., Irie, H., Kumar, V., Wagner, T., Schreier, S. F., Sinha, V., Wang, T., Wang, P., and Retscher, C.: Glyoxal tropospheric column retrievals from TROPOMI – multi-satellite intercomparison and ground-based validation, Atmos. Meas. Tech., 14, 7775–7807, https://doi.org/10.5194/amt-14-7775-2021, 2021.

Leung, D. M., Kok, J. F., Li, L., Lawrence, D. M., Mahowald, N. M., Tilmes, S., and Kluzek, E.: A global dust emission dataset for estimating dust radiative forcings in climate models, Atmos. Chem. Phys., 25, 2311–2331, https://doi.org/10.5194/acp-25-2311-2025, 2025.

Levelt, P. F., van den Oord, G. H. J., Dobber, M. R., Malkki, A., Visser, H., de Vries, J., Stammes, P., Lundell, J. O. V., and Saari, H.: The ozone monitoring instrument, IEEE Trans. Geosci. Remote Sens., 44, 1093–1101, https://doi.org/10.1109/TGRS.2006.872333, 2006.

Levy, R., Hsu, C., Sayer, A., Mattoo, S., and Lee, J.: MODIS Atmosphere L2 Aerosol Product. NASA MODIS Adaptive Processing System, https://doi.org/10.5067/MODIS/MOD04_L2.061; 10.5067/MODIS/MYD04_L2.061, 2017.

Levy, R. C., Mattoo, S., Munchak, L. A., Remer, L. A., Sayer, A. M., Patadia, F., and Hsu, N. C.: The Collection 6 MODIS aerosol products over land and ocean, Atmos. Meas. Tech., 6, 2989–3034, https://doi.org/10.5194/amt-6-2989-2013, 2013.

Levy, R. C., Munchak, L. A., Mattoo, S., Patadia, F., Remer, L. A., and Holz, R. E.: Towards a long-term global aerosol optical depth record: applying a consistent aerosol retrieval algorithm to MODIS and VIIRS-observed reflectance, Atmos. Meas. Tech., 8, 4083–4110, https://doi.org/10.5194/amt-8-4083-2015, 2015.

Li, C., Joiner, J., Krotkov, N. A., and Bhartia, P. K.: A fast and sensitive new satellite SO2 retrieval algorithm based on principal component analysis: Application to the ozone monitoring instrument, Geophys. Res. Lett., 40, 6314–6318, https://doi.org/10.1002/2013GL058134, 2013.

Li, C., Krotkov, N. A., Leonard, P., and Joiner, J.: OMI/Aura Sulphur Dioxide (SO2) Total Column 1-orbit L2 Swath 13x24 km V003, https://doi.org/10.5067/Aura/OMI/DATA2022, accessed: 2025/1/15, 2020a.

Li, C., Krotkov, N. A., Leonard, P. J. T., Carn, S., Joiner, J., Spurr, R. J. D., and Vasilkov, A.: Version 2 Ozone Monitoring Instrument SO_2 product (OMSO2 V2): new anthropogenic SO_2 vertical column density dataset, Atmos. Meas. Tech., 13, 6175–6191, https://doi.org/10.5194/amt-13-6175-2020, 2020b.

https://doi.org/10.5194/egusphere-2026-1681
Preprint. Discussion started: 27 April 2026

Li, H., Kalnay, E., and Miyoshi, T.: Simultaneous estimation of covariance inflation and observation errors within an ensemble Kalman filter, Q. J. R. Meteor. Soc., 135, 523–533, https://doi.org/10.1002/qj.371, 2009.

Li, J., Carlson, B. E., Yung, Y. L., Lv, D., Hansen, J., Penner, J. E., Liao, H., Ramaswamy, V., Kahn, R. A., Zhang, P., Dubovik, O., Ding, A., Lacis, A. A., Zhang, L., and Dong, Y.: Scattering and absorbing aerosols in the climate system, Nat. Rev. Earth Environ., 3, 363–379, https://doi.org/10.1038/s43017-022-00296-7, 2022a.

Li, L., Derimian, Y., Chen, C., Zhang, X., Che, H., Schuster, G. L., Fuertes, D., Litvinov, P., Lapyonok, T., Lopatin, A., Matar, C., Ducos, F., Karol, Y., Torres, B., Gui, K., Zheng, Y., Liang, Y., Lei, Y., Zhu, J., Zhang, L., Zhong, J., Zhang, X., and Dubovik, O.: Climatology of aerosol component concentrations derived from multi-angular polarimetric POLDER-3 observations using GRASP algorithm, Earth Syst. Sci. Data, 14, 3439–3469, https://doi.org/10.5194/essd-14-3439-2022, 2022b.

Liousse, C., Assamoi, E., Criqui, P., Granier, C., and Rosset, R.: Explosive growth in African combustion emissions from 2005 to 2030, Environ. Res. Lett., 9, 035 003, https://doi.org/10.1088/1748-9326/9/3/035003, 2014.

Livesey, N. J., Read, W. G., Froidevaux, L., Lambert, A., Manney, G. L., Pumphrey, H. C., Santee, M. L., Schwartz, M. J., Wang, S., Cofield, R. E., Cuddy, D. T., Fuller, R. A., Jarnot, R. F., Jiang, J. H., Knosp, B. W., Stek, P. C., Wagner, P. A., and Wu, D. L.: Aura Microwave Limb Sounder (MLS), Version 3.3 Level 2 data quality and description document, Tech. Rep. JPL D-33509, Jet Propulsion Laboratory, Pasadena, CA, available at https://mls.jpl.nasa.gov/data/v3-3_data_quality_document.pdf (last access: 22 August 2017), 2011.

Lu, S., Landgraf, J., Fu, G., van Diedenhoven, B., Wu, L., Rusli, S. P., and Hasekamp, O. P.: Simultaneous Retrieval of Trace Gases, Aerosols, and Cirrus Using RemoTAP—The Global Orbit Ensemble Study for the CO2M Mission, Front. Remote Sens., 3, https://doi.org/10.3389/frsen.2022.914378, 2022.

Luo, G., Yu, F., and Schwab, J.: Revised treatment of wet scavenging processes dramatically improves GEOS-Chem 12.0.0 simulations of surface nitric acid, nitrate, and ammonium over the United States, Geosci. Model Dev., 12, 3439–3447, https://doi.org/10.5194/gmd-12-3439-2019, 2019.

Luo, G., Yu, F., and Moch, J. M.: Further improvement of wet process treatments in GEOS-Chem v12.6.0: impact on global distributions of aerosols and aerosol precursors, Geosci. Model Dev., 13, 2879–2903, https://doi.org/10.5194/gmd-13-2879-2020, 2020.

Manney, G., Santee, M., Froidevaux, L., Livesey, N., and Read, W.: MLS/Aura Level 2 Nitric Acid (HNO3) Mixing Ratio V004, https://doi.org/10.5067/Aura/MLS/DATA2012, last accessed: 2025/1/16, 2015.

Marais, E. A. and Wiedinmyer, C.: Air Quality Impact of Diffuse and Inefficient Combustion Emissions in Africa (DICE-Africa), Environ. Sci. Tech., 50, 10 739–10 745, https://doi.org/10.1021/acs.est.6b02602, 2016.

Marais, E. A., Pandey, A. K., Van Damme, M., Clarisse, L., Coheur, P.-F., Shephard, M. W., Cady-Pereira, K. E., Misselbrook, T., Zhu, L., Luo, G., and Yu, F.: UK Ammonia Emissions Estimated With Satellite Observations and GEOS-Chem, J. Geophys. Res., 126, e2021JD035 237, https://doi.org/10.1029/2021JD035237, 2021.

Miller, D. O. and Brune, W. H.: Investigating the Understanding of Oxidation Chemistry Using 20 Years of Airborne OH and HO2 Observations, J. Geophys. Res., 127, e2021JD035 368, https://doi.org/https://doi.org/10.1029/2021JD035368, 2022.

Mitchell, H. L. and Houtekamer, P. L.: An Adaptive Ensemble Kalman Filter, Mon. Weather Rev., 128, 416–433, https://doi.org/10.1175/1520-0493(2000)128<0416:AAEKF>2.0.CO;2, 2000.

Miyazaki, K., Eskes, H., Sudo, K., Boersma, K. F., Bowman, K., and Kanaya, Y.: Decadal changes in global surface NO_x emissions from multi-constituent satellite data assimilation, Atmos. Chem. Phys., 17, 807–837, https://doi.org/10.5194/acp-17-807-2017, 2017.

Miyazaki, K., Sekiya, T., Fu, D., Bowman, K. W., Kulawik, S. S., Sudo, K., Walker, T., Kanaya, Y., Takigawa, M., Ogochi, K., Eskes, H., Boersma, K. F., Thompson, A. M., Gaubert, B., Barre, J., and Emmons, L. K.: Balance of Emission and Dynamical Controls on Ozone

https://doi.org/10.5194/egusphere-2026-1681
Preprint. Discussion started: 27 April 2026

During the Korea-United States Air Quality Campaign From Multiconstituent Satellite Data Assimilation, J. Geophys. Res., 124, 387–413, https://doi.org/10.1029/2018JD028912, 2019.

Miyazaki, K., Bowman, K., Sekiya, T., Eskes, H., Boersma, F., Worden, H., Livesey, N., Payne, V. H., Sudo, K., Kanaya, Y., Takigawa, M., and Ogochi, K.: Updated tropospheric chemistry reanalysis and emission estimates, TCR-2, for 2005–2018, Earth Syst. Sci. Data, 12, 2223–2259, https://doi.org/10.5194/essd-12-2223-2020, 2020a.

Miyazaki, K., Bowman, K. W., Yumimoto, K., Walker, T., and Sudo, K.: Evaluation of a multi-model, multi-constituent assimilation framework for tropospheric chemical reanalysis, Atmos. Chem. Phys., 20, 931–967, https://doi.org/10.5194/acp-20-931-2020, 2020b.

Miyazaki, K., Bowman, K., Sekiya, T., Takigawa, M., Neu, J. L., Sudo, K., Osterman, G., and Eskes, H.: Global tropospheric ozone responses to reduced NO_x emissions linked to the COVID-19 worldwide lockdowns, Sci. Adv., 7, eabf7460, https://doi.org/10.1126/sciadv.abf7460, 2021.

Murray, C. J. L., Aravkin, A. Y., Zheng, P., Abbafati, C., Abbas, K. M., and et al., M. A.-K.: Global burden of 87 risk factors in 204 countries and territories, 1990–2019: a systematic analysis for the Global Burden of Disease Study 2019, The Lancet, 396, 1223–1249, https://doi.org/10.1016/S0140-6736(20)30752-2, 2020.

Nenes, A., Pandis, S. N., and Pilinis, C.: ISORROPIA: A New Thermodynamic Equilibrium Model for Multiphase Multicomponent Inorganic Aerosols, Aquat. Geochem., 4, 123–152, https://doi.org/10.1023/A:1009604003981, 1998.

Oomen, G.-M., Müller, J.-F., Stavrakou, T., De Smedt, I., Blumenstock, T., Kivi, R., Makarova, M., Palm, M., Röhling, A., Té, Y., Vigouroux, C., Friedrich, M. M., Frieß, U., Hendrick, F., Merlaud, A., Piters, A., Richter, A., Van Roozendael, M., and Wagner, T.: Weekly derived top-down volatile-organic-compound fluxes over Europe from TROPOMI HCHO data from 2018 to 2021, Atmos. Chem. Phys., 24, 449–474, https://doi.org/10.5194/acp-24-449-2024, 2024.

O'Rourke, P., Smith, S. J., Mott, A. R., Ahsan, H., Mcduffie, E. E., Crippa, M., Klimont, Z., Mcdonald, B., Wang, S., Nicholson, M. B., Hoesly, R. M., and Feng, L.: CEDS v_2021_04_21 Gridded emissions data, https://doi.org/10.25584/PNNLDataHub/1779095, 2021.

Qu, Z., Henze, D. K., Worden, H. M., Jiang, Z., Gaubert, B., Theys, N., and Wang, W.: Sector-Based Top-Down Estimates of NO, SO2, and CO Emissions in East Asia, Geophys. Res. Lett., 49, e2021GL096 009, https://doi.org/10.1029/2021GL096009, 2022.

Radakovich, J. D., Houser, P. R., da Silva, A., and Bosilovich, M. G.: Results From Global Land-surface Data Assimilation Methods, in: AGU Spring Meeting Abstracts, vol. 2001, pp. H42E–07, 2001.

Randerson, J., van der Werf, G., Giglio, L., Collatz, G., and Kasibhatla, P.: Global Fire Emissions Database, Version 4.1 (GFEDv4), https://doi.org/10.3334/ORNLDAAC/1293, last access: January 31, 2025, 2018.

Randles, C. A., da Silva, A. M., Buchard, V., Colarco, P. R., Darmenov, A., Govindaraju, R., Smirnov, A., Holben, B., Ferrare, R., Hair, J., Shinozuka, Y., and Flynn, C. J.: The MERRA-2 Aerosol Reanalysis, 1980 Onward. Part I: System Description and Data Assimilation Evaluation, J. Clim., 30, 6823 – 6850, https://doi.org/10.1175/JCLI-D-16-0609.1, 2017.

Rayner, N. A., Parker, D. E., Horton, E. B., Folland, C. K., Alexander, L. V., Rowell, D. P., Kent, E. C., and Kaplan, A.: Global analyses of sea surface temperature, sea ice, and night marine air temperature since the late nineteenth century, J. Geophys. Res., 108, https://doi.org/10.1029/2002JD002670, 2003.

Remer, L. A., Kaufman, Y. J., Tanré, D., Mattoo, S., Chu, D. A., Martins, J. V., Li, R.-R., Ichoku, C., Levy, R. C., Kleidman, R. G., Eck, T. F., Vermote, E., and Holben, B. N.: The MODIS Aerosol Algorithm, Products, and Validation, J. Atmos. Sci., 62, 947–973, https://doi.org/10.1175/JAS3385.1, 2005.

https://doi.org/10.5194/egusphere-2026-1681
Preprint. Discussion started: 27 April 2026

Remer, L. A., Levy, R. C., Mattoo, S., Tanré, D., Gupta, P., Shi, Y., Sawyer, V., Munchak, L. A., Zhou, Y., Kim, M., Ichoku, C., Patadia, F., Li, R.-R., Gassó, S., Kleidman, R. G., and Holben, B. N.: The Dark Target Algorithm for Observing the Global Aerosol System: Past, Present, and Future, Remote Sens., 12, https://doi.org/10.3390/rs12182900, 2020.

Remer, L. A., Levy, R. C., and Martins, J. V.: Opinion: Aerosol remote sensing over the next 20 years, Atmos. Chem. Phys., 24, 2113–2127, https://doi.org/10.5194/acp-24-2113-2024, 2024.

Rijsdijk, P., Eskes, H., Dingemans, A., Boersma, K. F., Sekiya, T., Miyazaki, K., and Houweling, S.: Quantifying uncertainties in satellite NO_2 superobservations for data assimilation and model evaluation, Geosci. Model Dev., 18, 483–509, https://doi.org/10.5194/gmd-18-483-2025, 2025.

Sayer, A. M., Hsu, N. C., Bettenhausen, C., and Jeong, M.-J.: Validation and uncertainty estimates for MODIS Collection 6 "Deep Blue" aerosol data, J. Geophys. Res., 118, 7864–7872, https://doi.org/10.1002/jgrd.50600, 2013.

Sayer, A. M., Hsu, N. C., Bettenhausen, C., Jeong, M.-J., and Meister, G.: Effect of MODIS Terra radiometric calibration improvements on Collection 6 Deep Blue aerosol products: Validation and Terra/Aqua consistency, J. Geophys. Res., 120, 12,157–12,174, https://doi.org/10.1002/2015JD023878, 2015.

Sayer, A. M., Hsu, N. C., Lee, J., Bettenhausen, C., Kim, W. V., and Smirnov, A.: Satellite Ocean Aerosol Retrieval (SOAR) Algorithm Extension to S-NPP VIIRS as Part of the "Deep Blue" Aerosol Project, J. Geophys. Res., 123, 380–400, https://doi.org/10.1002/2017JD027412, 2018.

Schutgens, N., Nakata, M., and Nakajima, T.: Estimating Aerosol Emissions by Assimilating Remote Sensing Observations into a Global Transport Model, Remote Sens., 4, 3528–3543, https://doi.org/10.3390/rs4113528, 2012.

Schwartz, M., Froidevaux, L., Livesey, N., and Read, W.: MLS/Aura Level 2 Ozone (O3) Mixing Ratio V004, https://doi.org/10.5067/Aura/MLS/DATA2017, last accessed: 2025/1/16, 2015.

Sekiya, T., Miyazaki, K., Ogochi, K., Sudo, K., and Takigawa, M.: Global high-resolution simulations of tropospheric nitrogen dioxide using CHASER V4.0, Geosci. Model Dev., 11, 959–988, https://doi.org/10.5194/gmd-11-959-2018, 2018.

Sekiya, T., Miyazaki, K., Eskes, H., Sudo, K., Takigawa, M., and Kanaya, Y.: A comparison of the impact of TROPOMI and OMI tropospheric NO_2 on global chemical data assimilation, Atmos. Meas. Tech., 15, 1703–1728, https://doi.org/10.5194/amt-15-1703-2022, 2022.

Sekiya, T., Miyazaki, K., Eskes, H., Bowman, K., Sudo, K., Kanaya, Y., and Takigawa, M.: The worldwide COVID-19 lockdown impacts on global secondary inorganic aerosols and radiative budget, Sci. Adv., 9, eadh2688, https://doi.org/10.1126/sciadv.adh2688, 2023.

Shah, V., Keller, C. A., Knowland, K. E., Christiansen, A., Hu, L., Wang, H., Lu, X., Alexander, B., and Jacob, D. J.: Particulate Nitrate Photolysis as a Possible Driver of Rising Tropospheric Ozone, Geophys. Res. Lett., 51, e2023GL107 980, https://doi.org/https://doi.org/10.1029/2023GL107980, 2024.

Shephard, M. W. and Cady-Pereira, K. E.: Cross-track Infrared Sounder (CrIS) satellite observations of tropospheric ammonia, Atmos. Meas. Tech., 8, 1323–1336, https://doi.org/10.5194/amt-8-1323-2015, 2015.

Sickles, J. E. and Shadwick, D. S.: Precision of atmospheric dry deposition data from the Clean Air Status and Trends Network, Atmos. Environ., 36, 5671–5686, https://doi.org/10.1016/S1352-2310(02)00723-9, 2002.

Simpson, D., Benedictow, A., and Darras, S.: CAMS-GLOB-SOIL. In CAMS2_61 – Global and European Emission Inventories. Documentation of CAMS Emission Inventory Products, Tech. rep., Copernicus Atmosphere Monitoring Service, https://doi.org/10.24380/q2si-ti6i, 2023.

https://doi.org/10.5194/egusphere-2026-1681
Preprint. Discussion started: 27 April 2026

Sinyuk, A., Holben, B. N., Eck, T. F., Giles, D. M., Slutsker, I., Korkin, S., Schafer, J. S., Smirnov, A., Sorokin, M., and Lyapustin, A.: The AERONET Version 3 aerosol retrieval algorithm, associated uncertainties and comparisons to Version 2, Atmos. Meas. Tech., 13, 3375–3411, https://doi.org/10.5194/amt-13-3375-2020, 2020.

Smith, C. J., Kramer, R. J., Myhre, G., Alterskjær, K., Collins, W., Sima, A., Boucher, O., Dufresne, J.-L., Nabat, P., Michou, M., Yukimoto, S., Cole, J., Paynter, D., Shiogama, H., O'Connor, F. M., Robertson, E., Wiltshire, A., Andrews, T., Hannay, C., Miller, R., Nazarenko, L., Kirkevåg, A., Olivié, D., Fiedler, S., Lewinschal, A., Mackallah, C., Dix, M., Pincus, R., and Forster, P. M.: Effective radiative forcing and adjustments in CMIP6 models, Atmos. Chem. Phys., 20, 9591–9618, https://doi.org/10.5194/acp-20-9591-2020, 2020.

Sudo, K., Takahashi, M., Kurokawa, J.-i., and Akimoto, H.: CHASER: A global chemical model of the troposphere 1. Model description, J. Geophys. Res., 107, ACH 7–1–ACH 7–20, https://doi.org/https://doi.org/10.1029/2001JD001113, 2002.

Takemura, T., Okamoto, H., Maruyama, Y., Numaguti, A., Higurashi, A., and Nakajima, T.: Global three-dimensional simulation of aerosol optical thickness distribution of various origins, J. Geophys. Res., 105, 17 853–17 873, https://doi.org/https://doi.org/10.1029/2000JD900265, 2000.

Takemura, T., Nakajima, T., Dubovik, O., Holben, B. N., and Kinne, S.: Single-Scattering Albedo and Radiative Forcing of Various Aerosol Species with a Global Three-Dimensional Model, J. Clim., 15, 333–352, https://doi.org/10.1175/1520-0442(2002)015<0333:SSAARF>2.0.CO;2, 2002.

Tang, I. N. and Munkelwitz, H. R.: Water activities, densities, and refractive indices of aqueous sulfates and sodium nitrate droplets of atmospheric importance, J. Geophys. Res., 99, 18 801–18 808, https://doi.org/10.1029/94JD01345, 1994.

Tanré, D., Bréon, F. M., Deuzé, J. L., Dubovik, O., Ducos, F., François, P., Goloub, P., Herman, M., Lifermann, A., and Waquet, F.: Remote sensing of aerosols by using polarized, directional and spectral measurements within the A-Train: the PARASOL mission, Atmos. Meas. Tech., 4, 1383–1395, https://doi.org/10.5194/amt-4-1383-2011, 2011.

Theys, N. and Vlietinck, J.: S5P COBRA Sulphur Dioxide [L2__SO2CBR_] Readme, Tech. Rep. S5P-BIRA-PRF-SO2CBR, European Space Agency, https://data-portal.s5p-pal.com/product-docs/so2cbr/S5P-BIRA-PRF-SO2CBR_2.2.pdf, last access: 2025/1/15, 2024.

Theys, N., Fioletov, V., Li, C., De Smedt, I., Lerot, C., McLinden, C., Krotkov, N., Griffin, D., Clarisse, L., Hedelt, P., Loyola, D., Wagner, T., Kumar, V., Innes, A., Ribas, R., Hendrick, F., Vlietinck, J., Brenot, H., and Van Roozendael, M.: A sulfur dioxide Covariance-Based Retrieval Algorithm (COBRA): application to TROPOMI reveals new emission sources, Atmos. Chem. Phys., 21, 16 727–16 744, https://doi.org/10.5194/acp-21-16727-2021, 2021.

Thurston, G. D., Burnett, R. T., Turner, M. C., Shi, Y., Krewski, D., Lall, R., Ito, K., Jerrett, M., Gapstur, S. M., Diver, W. R., and Pope, C. A.: Ischemic Heart Disease Mortality and Long-Term Exposure to Source-Related Components of U.S. Fine Particle Air Pollution, Environ. Health Perspect., 124, 785–794, https://doi.org/10.1289/ehp.1509777, 2016.

Tilmes, S., Mills, M. J., Zhu, Y., Bardeen, C. G., Vitt, F., Yu, P., Fillmore, D., Liu, X., Toon, B., and Deshler, T.: Description and performance of a sectional aerosol microphysical model in the Community Earth System Model (CESM2), Geosci. Model Dev., 16, 6087–6125, https://doi.org/10.5194/gmd-16-6087-2023, 2023.

Titos, G., Burgos, M. A., Zieger, P., Alados-Arboledas, L., Baltensperger, U., Jefferson, A., Sherman, J., Weingartner, E., Henzing, B., Luoma, K., O'Dowd, C., Wiedensohler, A., and Andrews, E.: A global study of hygroscopicity-driven light-scattering enhancement in the context of other in situ aerosol optical properties, Atmos. Chem. Phys., 21, 13 031–13 050, https://doi.org/10.5194/acp-21-13031-2021, 2021.

Tsikerdekis, A., Hasekamp, O. P., Schutgens, N. A. J., and Zhong, Q.: Assimilation of POLDER observations to estimate aerosol emissions, Atmos. Chem. Phys., 23, 9495–9524, https://doi.org/10.5194/acp-23-9495-2023, 2023.

https://doi.org/10.5194/egusphere-2026-1681
Preprint. Discussion started: 27 April 2026

Ueda, K., Yamagami, M., Ikemori, F., Hisatsune, K., and Nitta, H.: Associations Between Fine Particulate Matter Components and Daily Mortality in Nagoya, Japan, J. Epidemiol., 26, 249–257, https://doi.org/10.2188/jea.JE20150039, 2016.

Van Damme, M., Clarisse, L., Heald, C. L., Hurtmans, D., Ngadi, Y., Clerbaux, C., Dolman, A. J., Erisman, J. W., and Coheur, P. F.: Global distributions, time series and error characterization of atmospheric ammonia (NH_3) from IASI satellite observations, Atmos. Chem. Phys., 14, 2905–2922, https://doi.org/10.5194/acp-14-2905-2014, 2014.

van der A, R. J., Ding, J., and Eskes, H.: Monitoring European anthropogenic NO_x emissions from space, Atmos. Chem. Phys., 24, 7523–7534, https://doi.org/10.5194/acp-24-7523-2024, 2024.

van Geffen, J., Boersma, K. F., Eskes, H., Sneep, M., ter Linden, M., Zara, M., and Veefkind, J. P.: S5P TROPOMI NO_2 slant column retrieval: method, stability, uncertainties and comparisons with OMI, Atmos. Meas. Tech., 13, 1315–1335, https://doi.org/10.5194/amt-13-1315-2020, 2020.

van Geffen, J., Eskes, H., Compernolle, S., Pinardi, G., Verhoelst, T., Lambert, J.-C., Sneep, M., ter Linden, M., Ludewig, A., Boersma, K. F., and Veefkind, J. P.: Sentinel-5P TROPOMI NO_2 retrieval: impact of version v2.2 improvements and comparisons with OMI and ground-based data, Atmos. Meas. Tech., 15, 2037–2060, https://doi.org/10.5194/amt-15-2037-2022, 2022.

van Zadelhoff, G.-J., Donovan, D. P., and Wang, P.: Detection of aerosol and cloud features for the EarthCARE atmospheric lidar (ATLID): the ATLID FeatureMask (A-FM) product, Atmos. Meas. Tech., 16, 3631–3651, https://doi.org/10.5194/amt-16-3631-2023, 2023.

Veefkind, J., Aben, I., McMullan, K., Förster, H., de Vries, J., Otter, G., Claas, J., Eskes, H., de Haan, J., Kleipool, Q., van Weele, M., Hasekamp, O., Hoogeveen, R., Landgraf, J., Snel, R., Tol, P., Ingmann, P., Voors, R., Kruizinga, B., Vink, R., Visser, H., and Levelt, P.: TROPOMI on the ESA Sentinel-5 Precursor: A GMES mission for global observations of the atmospheric composition for climate, air quality and ozone layer applications, Rem. Sens. Env., 120, 70 – 83, https://doi.org/10.1016/j.rse.2011.09.027, 2012.

Wang, Z., Lin, L., Xu, Y., Che, H., Zhang, X., Zhang, H., Dong, W., Wang, C., Gui, K., and Xie, B.: Incorrect Asian aerosols affecting the attribution and projection of regional climate change in CMIP6 models, npj Clim. Atmos. Sci., 4, 2, https://doi.org/10.1038/s41612-020-00159-2, 2021.

Weichenthal, S., Christidis, T., Olaniyan, T., van Donkelaar, A., Martin, R., Tjepkema, M., Burnett, R. T., and Brauer, M.: Epidemiological studies likely need to consider PM2.5 composition even if total outdoor PM2.5 mass concentration is the exposure of interest, Environ. Epidemiol., 8, https://doi.org/10.1097/EE9.0000000000000317, 2024.

Weinheimer, A. J., Walega, J. G., Ridley, B. A., Sachse, G. W., Anderson, B. E., and Collins Jr., J. E.: Stratospheric NOy measurements on the NASA DC-8 during AASE II, Geophys. Res. Lett., 20, 2563–2566, https://doi.org/10.1029/93GL02627, 1993.

Wells, K. C., Millet, D. B., Payne, V. H., Vigouroux, C., Aquino, C. A. B., De Mazière, M., de Gouw, J. A., Graus, M., Kurosu, T., Warneke, C., and Wisthaler, A.: Next-Generation Isoprene Measurements From Space: Detecting Daily Variability at High Resolution, J. Geophys. Res., 127, e2021JD036 181, https://doi.org/10.1029/2021JD036181, 2022.

Winker, D. M., Tackett, J. L., Getzewich, B. J., Liu, Z., Vaughan, M. A., and Rogers, R. R.: The global 3-D distribution of tropospheric aerosols as characterized by CALIOP, Atmos. Chem. Phys., 13, 3345–3361, https://doi.org/10.5194/acp-13-3345-2013, 2013.

Wofsy, S., Afshar, S., Allen, H., Apel, E., Asher, E., Barletta, B., Bent, J., Bian, H., Biggs, B., Blake, D., Blake, N., Bourgeois, I., Brock, C., Brune, W., Budney, J., Bui, T., Butler, A., Campuzano-Jost, P., Chang, C., Chin, M., Commane, R., Correa, G., Crounse, J., Cullis, P. D., Daube, B., Day, D., Dean-Day, J., Dibb, J., DiGangi, J., Diskin, G., Dollner, M., Elkins, J., Erdesz, F., Fiore, A., Flynn, C., Froyd, K., Gesler, D., Hall, S., Hanisco, T., Hannun, R., Hills, A., Hintsa, E., Hoffman, A., Hornbrook, R., Huey, L., Hughes, S., Jimenez, J., Johnson, B., Katich, J., Keeling, R., Kim, M., Kupc, A., Lait, L., Lamarque, J.-F., Liu, J., McKain, K., Mclaughlin, R., Meinardi, S., Miller, D., Montzka, S., Moore, F., Morgan, E., Murphy, D., Murray, L., Nault, B., Neuman, J., Newman, P., Nicely, J., Pan, X., Paplawsky, W.,

https://doi.org/10.5194/egusphere-2026-1681
Preprint. Discussion started: 27 April 2026

Peischl, J., Prather, M., Price, D., Ray, E., Reeves, J., Richardson, M., Rollins, A., Rosenlof, K., Ryerson, T., Scheuer, E., Schill, G., Schroder, J., Schwarz, J., St.Clair, J., Steenrod, S., Stephens, B., Strode, S., Sweeney, C., Tanner, D., Teng, A., Thames, A., Thompson, C., Ullmann, K., Veres, P., Vieznor, N., Wagner, N., Watt, A., Weber, R., Weinzierl, B., Wennberg, P., Williamson, C., Wilson, J., Wolfe, G., Woods, C., and Zeng, L.: ATom: Merged Atmospheric Chemistry, Trace Gases, and Aerosols, https://doi.org/10.3334/ORNLDAAC/1581, 2018.

Xue, T., Zheng, Y., Li, X., Liu, J., Zhang, Q., and Zhu, T.: A component-specific exposure–mortality model for ambient PM2.5 in China: findings from nationwide epidemiology based on outputs from a chemical transport model, Faraday Discuss., 226, 551–568, https://doi.org/10.1039/D0FD00093K, 2021.

Yienger, J. J. and Levy II, H.: Empirical model of global soil-biogenic NOχ emissions, J. Geophys. Res., 100, 11 447–11 464, https://doi.org/https://doi.org/10.1029/95JD00370, 1995.

Yu, F., Luo, G., and Ma, X.: Regional and global modeling of aerosol optical properties with a size, composition, and mixing state resolved particle microphysics model, Atmos. Chem. Phys., 12, 5719–5736, https://doi.org/10.5194/acp-12-5719-2012, 2012.

Yumimoto, K. and Takemura, T.: Long-term inverse modeling of Asian dust: Interannual variations of its emission, transport, deposition, and radiative forcing, J. Geophys. Res., 120, 1582–1607, https://doi.org/10.1002/2014JD022390, 2015.

Yumimoto, K., Tanaka, T. Y., Oshima, N., and Maki, T.: JRAero: the Japanese Reanalysis for Aerosol v1.0, Geosci. Model Dev., 10, 3225–3253, https://doi.org/10.5194/gmd-10-3225-2017, 2017.

Zhai, S., Jacob, D. J., Brewer, J. F., Li, K., Moch, J. M., Kim, J., Lee, S., Lim, H., Lee, H. C., Kuk, S. K., Park, R. J., Jeong, J. I., Wang, X., Liu, P., Luo, G., Yu, F., Meng, J., Martin, R. V., Travis, K. R., Hair, J. W., Anderson, B. E., Dibb, J. E., Jimenez, J. L., Campuzano-Jost, P., Nault, B. A., Woo, J.-H., Kim, Y., Zhang, Q., and Liao, H.: Relating geostationary satellite measurements of aerosol optical depth (AOD) over East Asia to fine particulate matter ($PM_{2.5}$): insights from the KORUS-AQ aircraft campaign and GEOS-Chem model simulations, Atmos. Chem. Phys., 21, 16 775–16 791, https://doi.org/10.5194/acp-21-16775-2021, 2021.

Zhong, Q., Schutgens, N., van der Werf, G. R., van Noije, T., Bauer, S. E., Tsigaridis, K., Mielonen, T., Checa-Garcia, R., Neubauer, D., Kipling, Z., Kirkevåg, A., Olivié, D. J. L., Kokkola, H., Matsui, H., Ginoux, P., Takemura, T., Le Sager, P., Rémy, S., Bian, H., and Chin, M.: Using modelled relationships and satellite observations to attribute modelled aerosol biases over biomass burning regions, Nat. Comm., 13, 5914, https://doi.org/10.1038/s41467-022-33680-4, 2022.

Zhu, L., Henze, D., Bash, J., Jeong, G.-R., Cady-Pereira, K., Shephard, M., Luo, M., Paulot, F., and Capps, S.: Global evaluation of ammonia bidirectional exchange and livestock diurnal variation schemes, Atmos. Chem. Phys., 15, 12 823–12 843, https://doi.org/10.5194/acp-15-12823-2015, 2015.

https://doi.org/10.5194/egusphere-2026-1681
Preprint. Discussion started: 27 April 2026

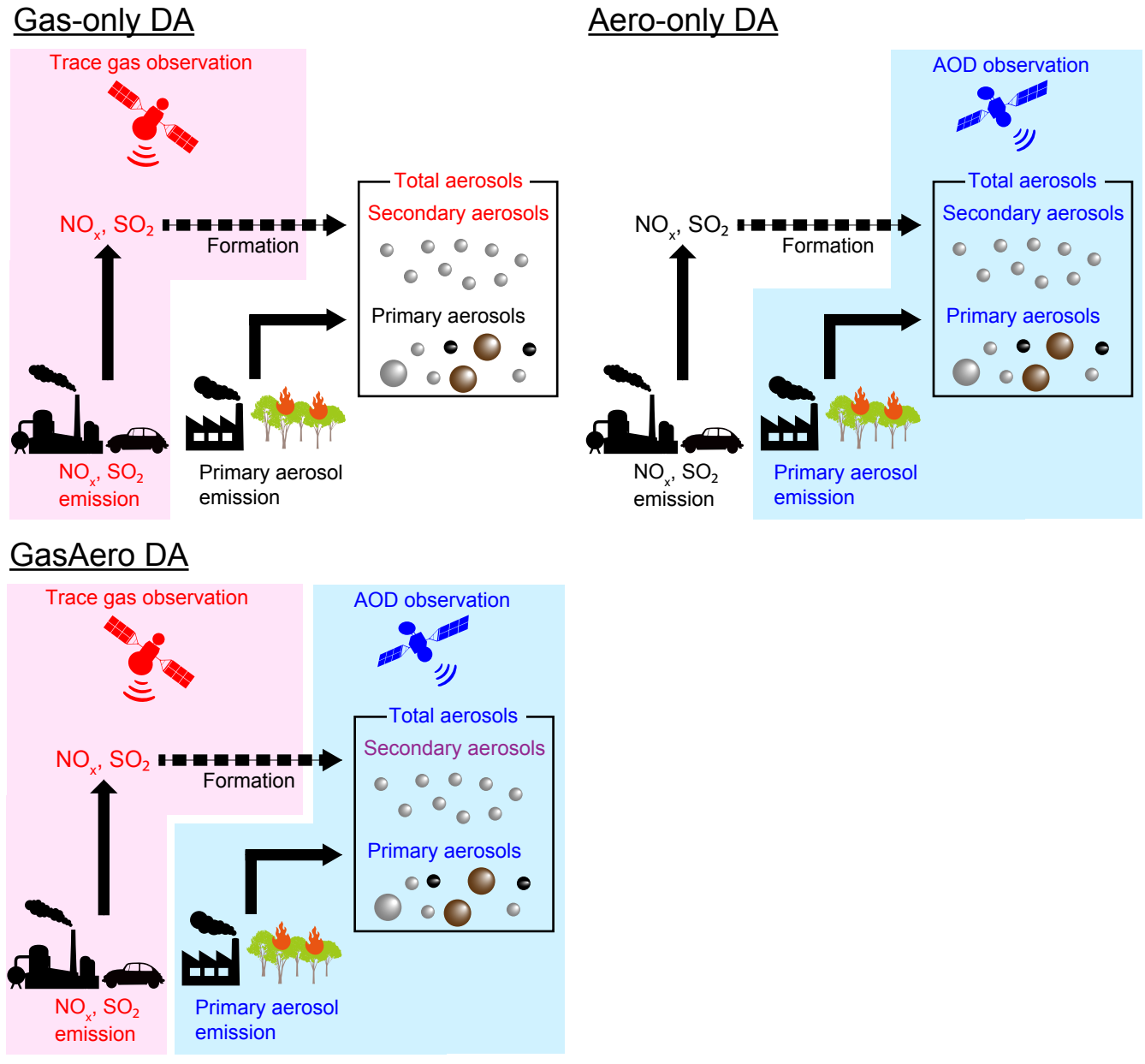

Figure 1. Schematic diagram of simultaneous data assimilation of trace gas and AOD observations (GasAero DA), conventional data assimilation of trace gas observations (Gas-only DA) and AOD observations separately (Aero-only DA). The solid and dashed arrows indicate direct emissions and chemical formation, respectively. Red, blue, and purple characters denote the variables influenced by trace gas assimilation, AOD assimilation, and both trace gas and AOD assimilation, respectively.

https://doi.org/10.5194/egusphere-2026-1681
Preprint. Discussion started: 27 April 2026

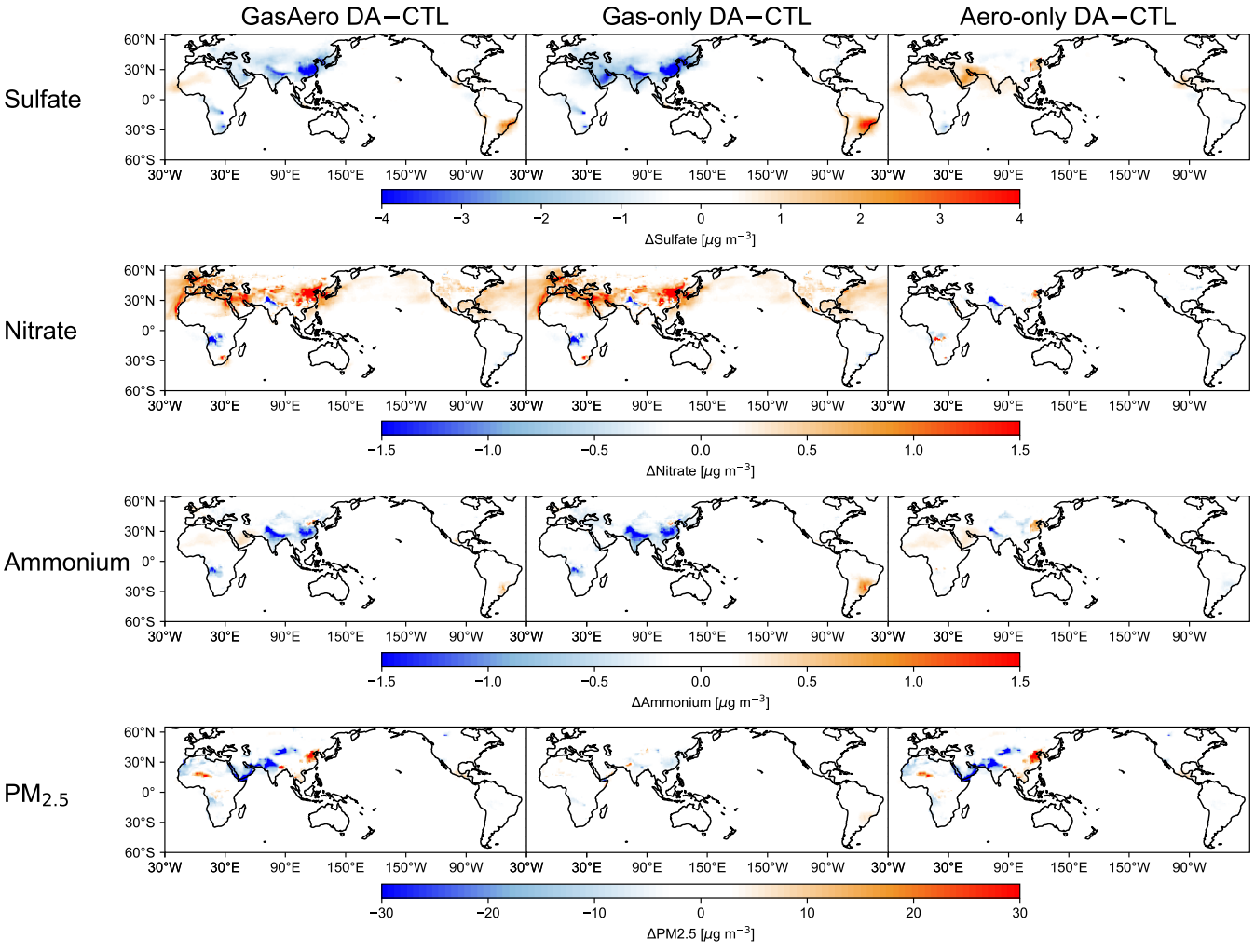

Figure 2. Surface sulfate (first row), nitrate (second row), ammonium (third row), and fine particulate matters ($PM_{2.5}$; fourth row) concentration changes due to data assimilation during May–August 2016, compared to the control simulation. The left column is the concentration changes due to the simultaneous DA of trace gases and AOD observations (GasAero DA). The center and right columns are conventional DAs of trace gas observations (Gas-only DA) and AOD observations (Aero-only DA), respectively. The unit is μg m^{-3}.

https://doi.org/10.5194/egusphere-2026-1681
Preprint. Discussion started: 27 April 2026

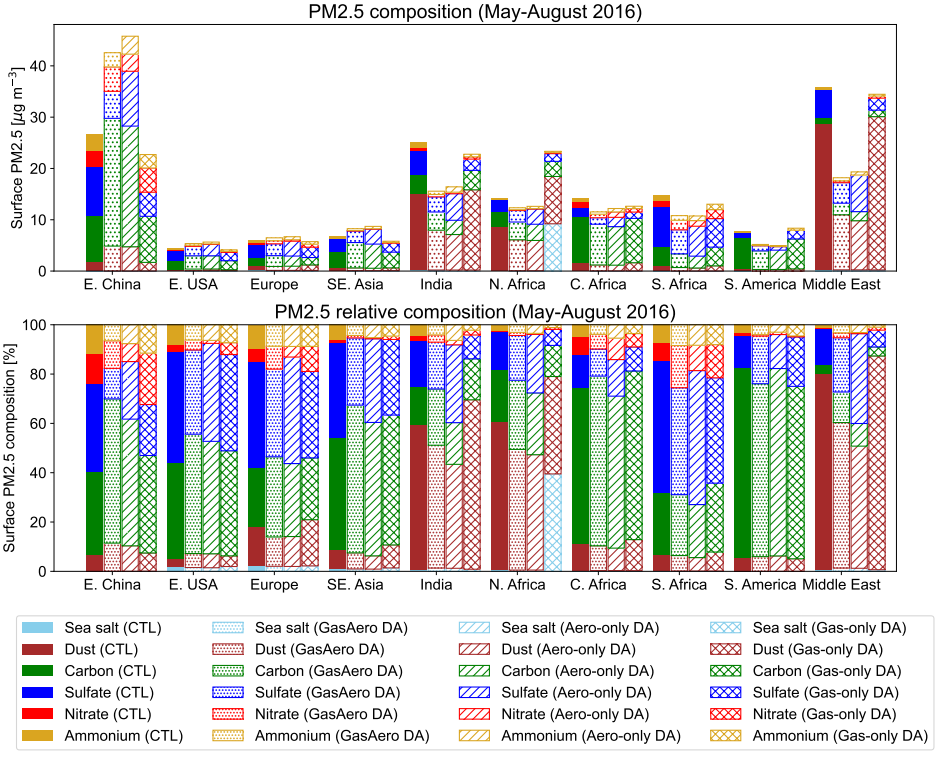

Figure 3. Regional mean concentrations of fine particulate matters ($PM_{2.5}$) composition (top) and relative composition (bottom) during May–August 2016. The bars with no hatch, dotted hatch, diagonal hatch, and cross hatch indicate the control simulation, the GasAero DA, the Aero-only DA, and the Gas-only DA, respectively. Sky blue, brown, green, blue, red, and yellow colors denote sea salt, dust, carbonaceous, sulfate, nitrate, and ammonium aerosols, respectively. The unit is $\mu g\ m^{-3}$. Region definition is shown in Fig. S5.

https://doi.org/10.5194/egusphere-2026-1681
Preprint. Discussion started: 27 April 2026

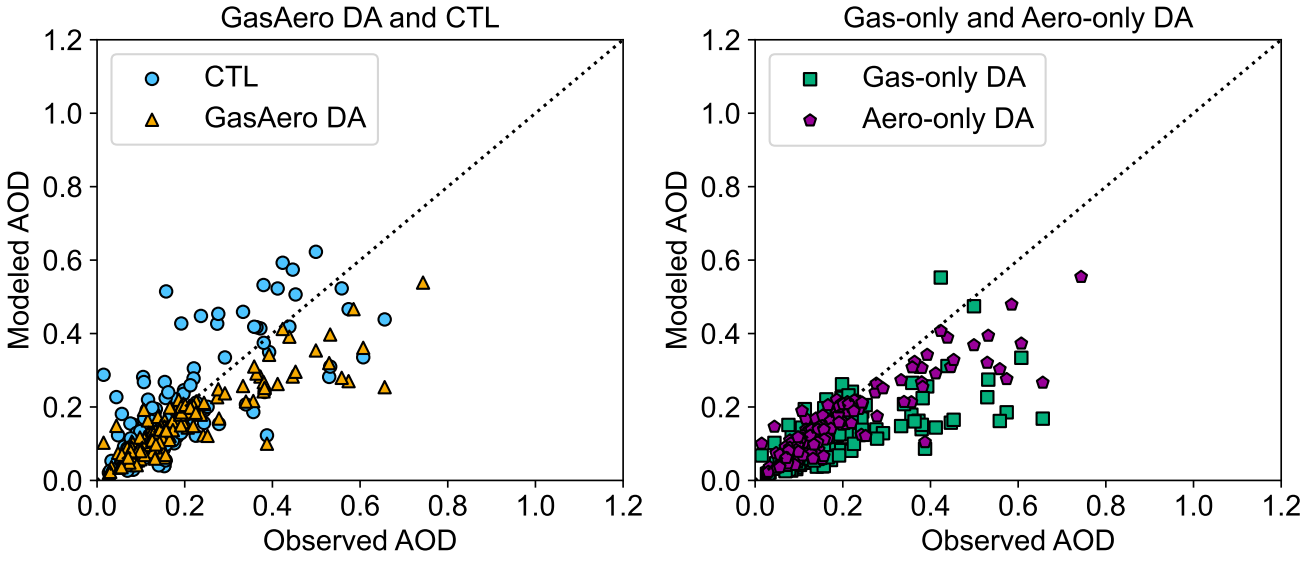

Figure 4. Scatter plot of observed aerosol optical depth (AOD) derived from AERONET with analyzed AOD derived from the control simulation (skyblue circle), the GasAero DA (orange triangle), Gas-only DA (green square), and Aero-only DA (purple hexagon) during May–August 2016. The observation sites were selected by the criteria of >25% temporal coverage during May–August 2016. The dotted line indicates the 1:1 line.

https://doi.org/10.5194/egusphere-2026-1681
Preprint. Discussion started: 27 April 2026

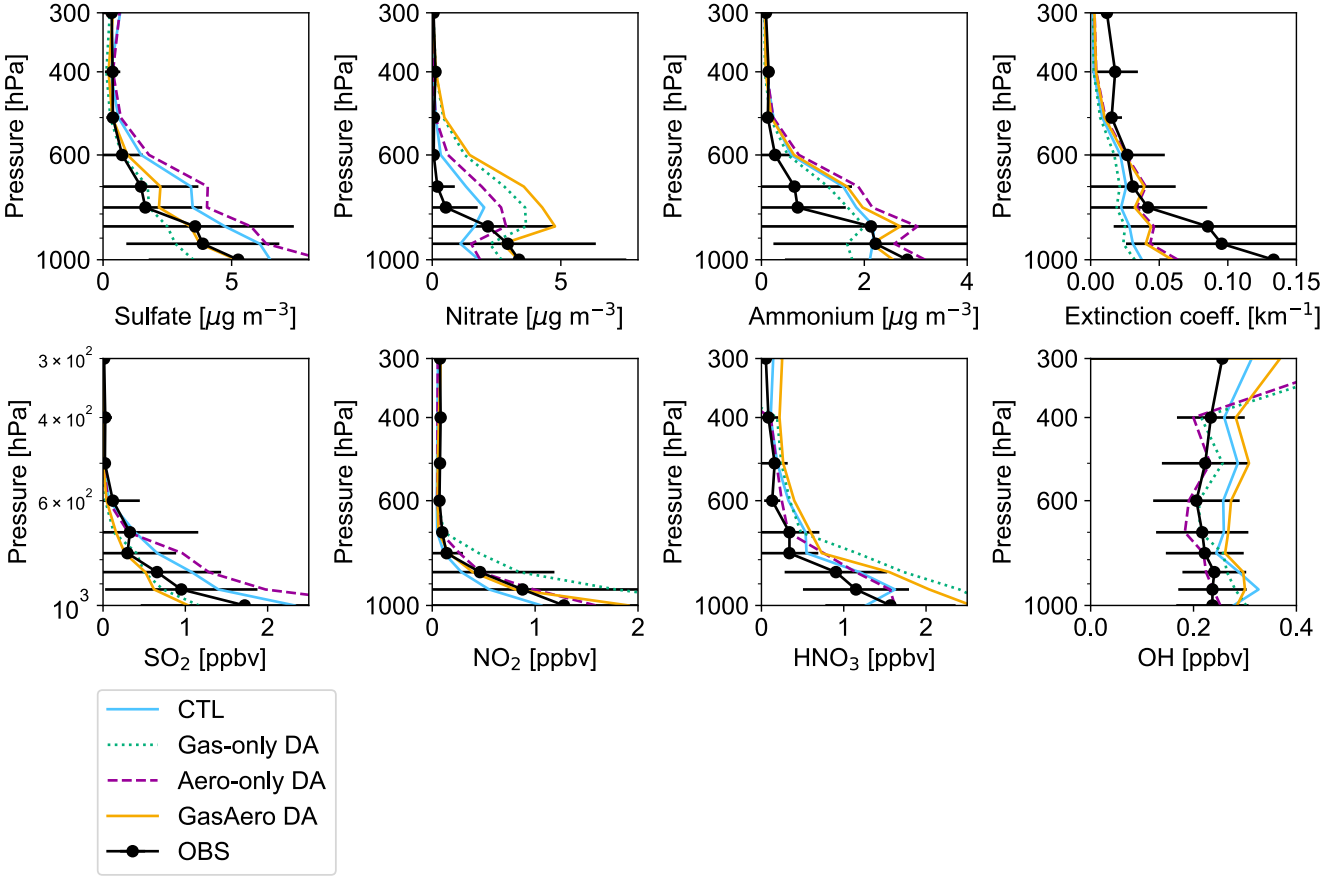

Figure 5. Vertical profiles of aerosols (sulfate, nitrate, ammonium, total extinction coefficients; from first to fourth columns, respectively, on the top panels) and trace gas species (sulfur dioxide, nitrogen dioxide, nitric acid, and hydroxyl radicals; from first to fourth columns, respectively, on the bottom panels) during the KORUS-AQ aircraft-campaign observations. The black line with circle represents observations, the skyblue solid, orange solid, green dotted, and purple dashed lines are the control simulation, GasAero DA, Gas-only DA, and Aero-only DA, respectively. The units are μg m^{-3} for aerosols, km^{-1} for total extinction coefficients, and part per billion volume (ppbv) for trace gases.

https://doi.org/10.5194/egusphere-2026-1681
Preprint. Discussion started: 27 April 2026

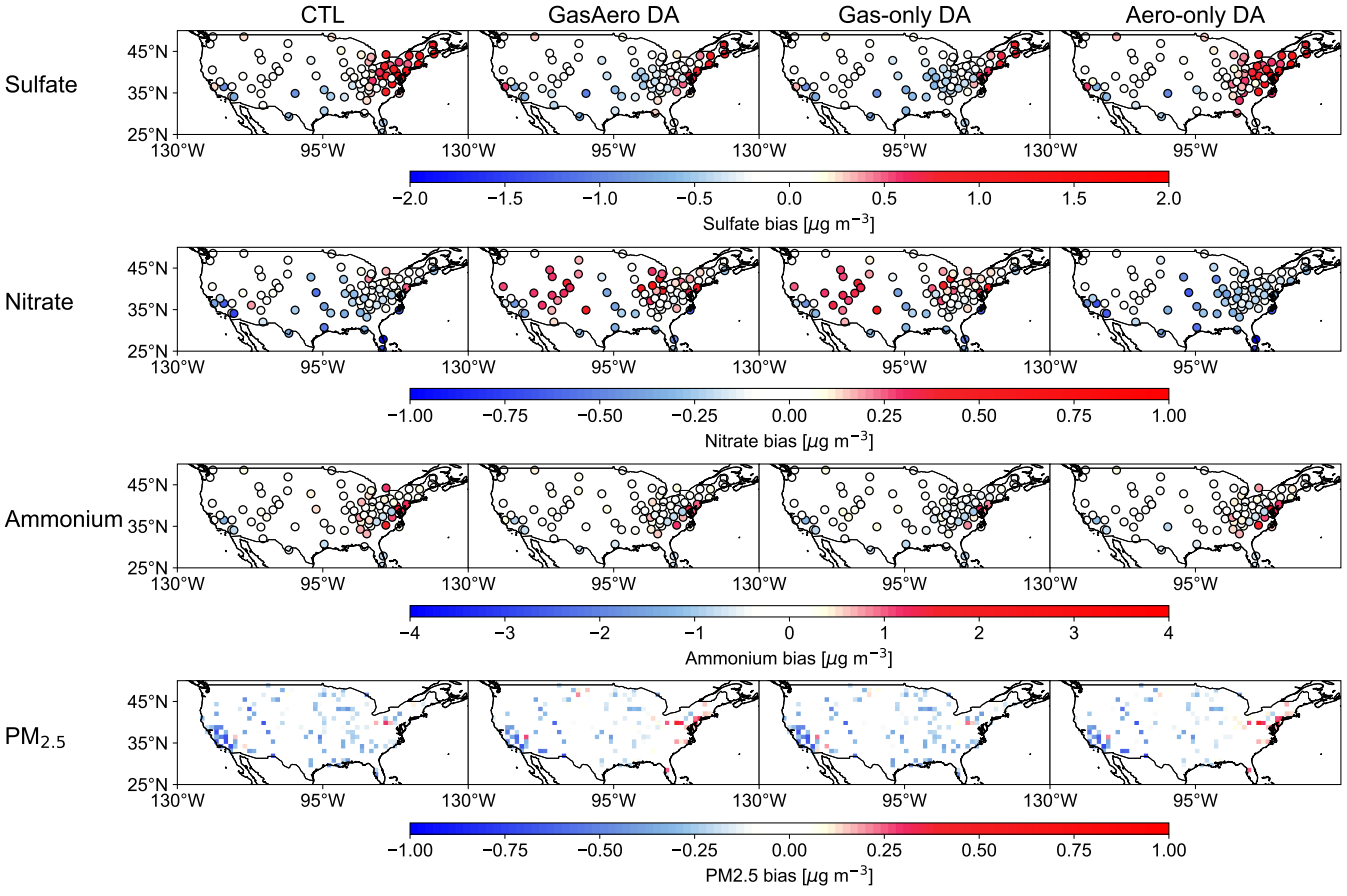

Figure 6. Spatial maps of mean biases of sulfate (first row), nitrate (second row), ammonium (third row), and fine particulate matters ($PM_{2.5}$; fourth row) in the control simulation (first column), GasAero DA (second column), Gas-only DA (third column), and Aero-only DA (fourth column) over the United States during May–August 2016. The unit is $\mu g\ m^{-3}$.

https://doi.org/10.5194/egusphere-2026-1681
Preprint. Discussion started: 27 April 2026

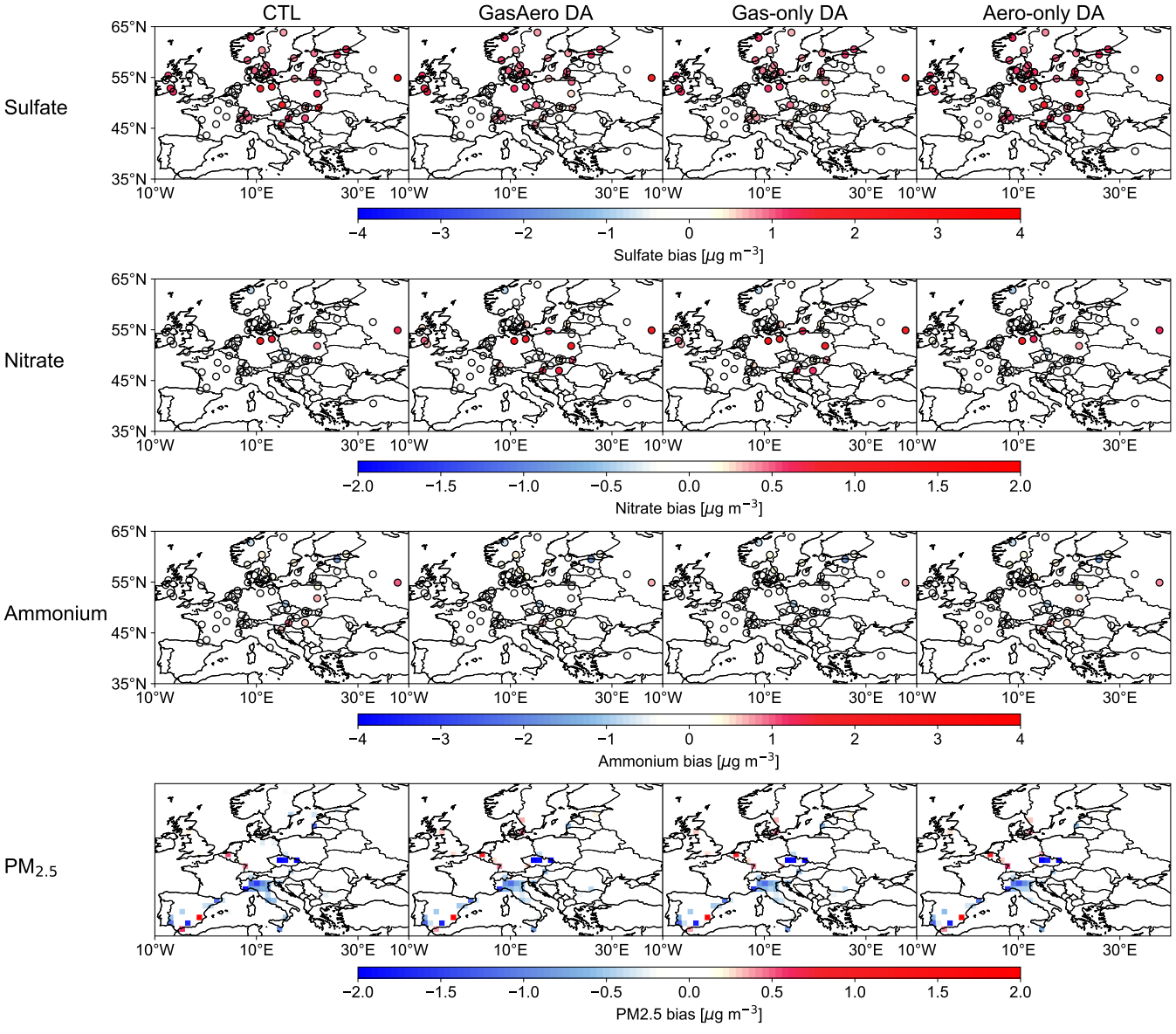

Figure 7. Spatial maps of mean biases of sulfate (first row), nitrate (second row), ammonium (third row), and fine particulate matters ($PM_{2.5}$; fourth row) in the control simulation (first column), GasAero DA (second column), Gas-only DA (third column), and Aero-only DA (fourth column) over Europe during May–August 2016. The unit is $\mu g\ m^{-3}$.

https://doi.org/10.5194/egusphere-2026-1681
Preprint. Discussion started: 27 April 2026

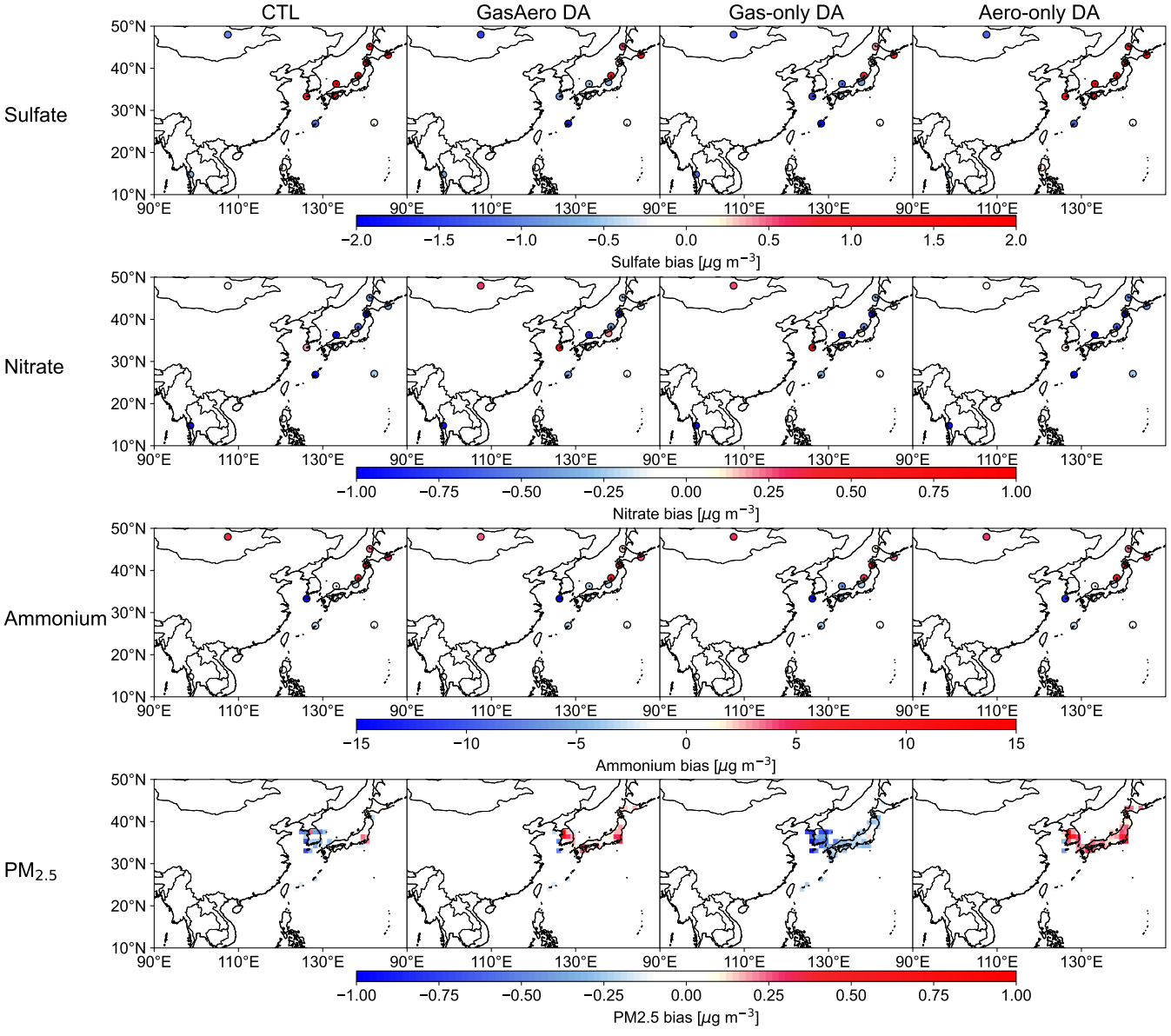

Figure 8. Spatial maps of mean biases of sulfate (first row), nitrate (second row), ammonium (third row), and fine particulate matters ($PM_{2.5}$; fourth row) in the control simulation (first column), GasAero DA (second column), Gas-only DA (third column), and Aero-only DA (fourth column) over Asia during May–August 2016. The unit is $\mu g\ m^{-3}$.

https://doi.org/10.5194/egusphere-2026-1681
Preprint. Discussion started: 27 April 2026

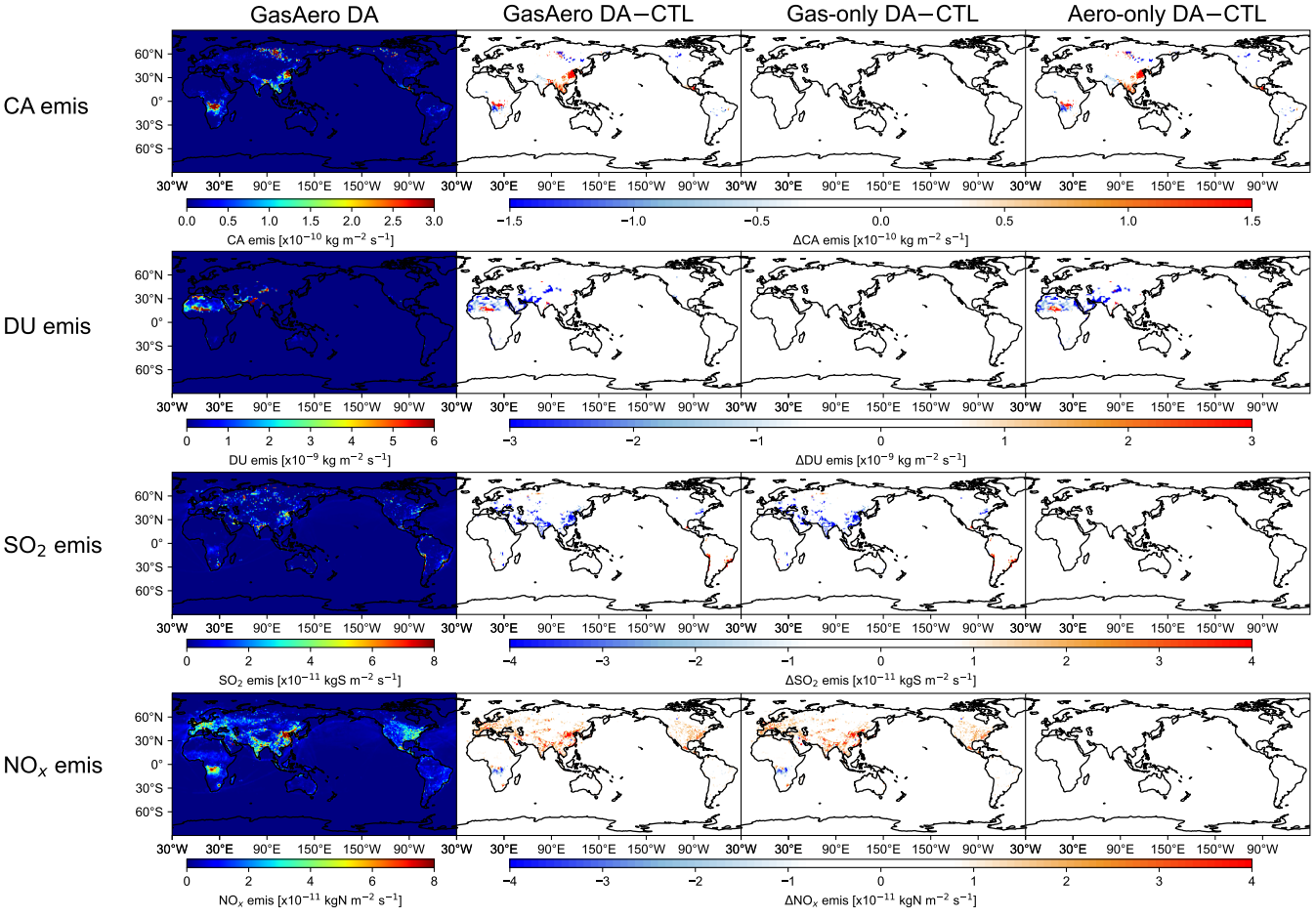

Figure 9. Mean surface emissions of carbonaceous aerosols (first row), mineral dust (second row), sulfur dioxide (SO_2; third row), and nitrogen oxides (NO_x; fourth row) in the GasAero DA (first column) and their changes made to the GasAero DA (second column), Gas-only DA (third column), and Aero-only DA (fourth column), compared to the control simulation, during May–August 2016. The units are $\times 10^{-10}$ kg m^{-2} s^{-1} for carbonaceous aerosols, $\times 10^{-9}$ kg m^{-2} s^{-1} for mineral dust, $\times 10^{-11}$ kg S m^{-2} s^{-1} for SO_2, and $\times 10^{-11}$ kg N m^{-2} s^{-1} for NO_x.

https://doi.org/10.5194/egusphere-2026-1681
Preprint. Discussion started: 27 April 2026

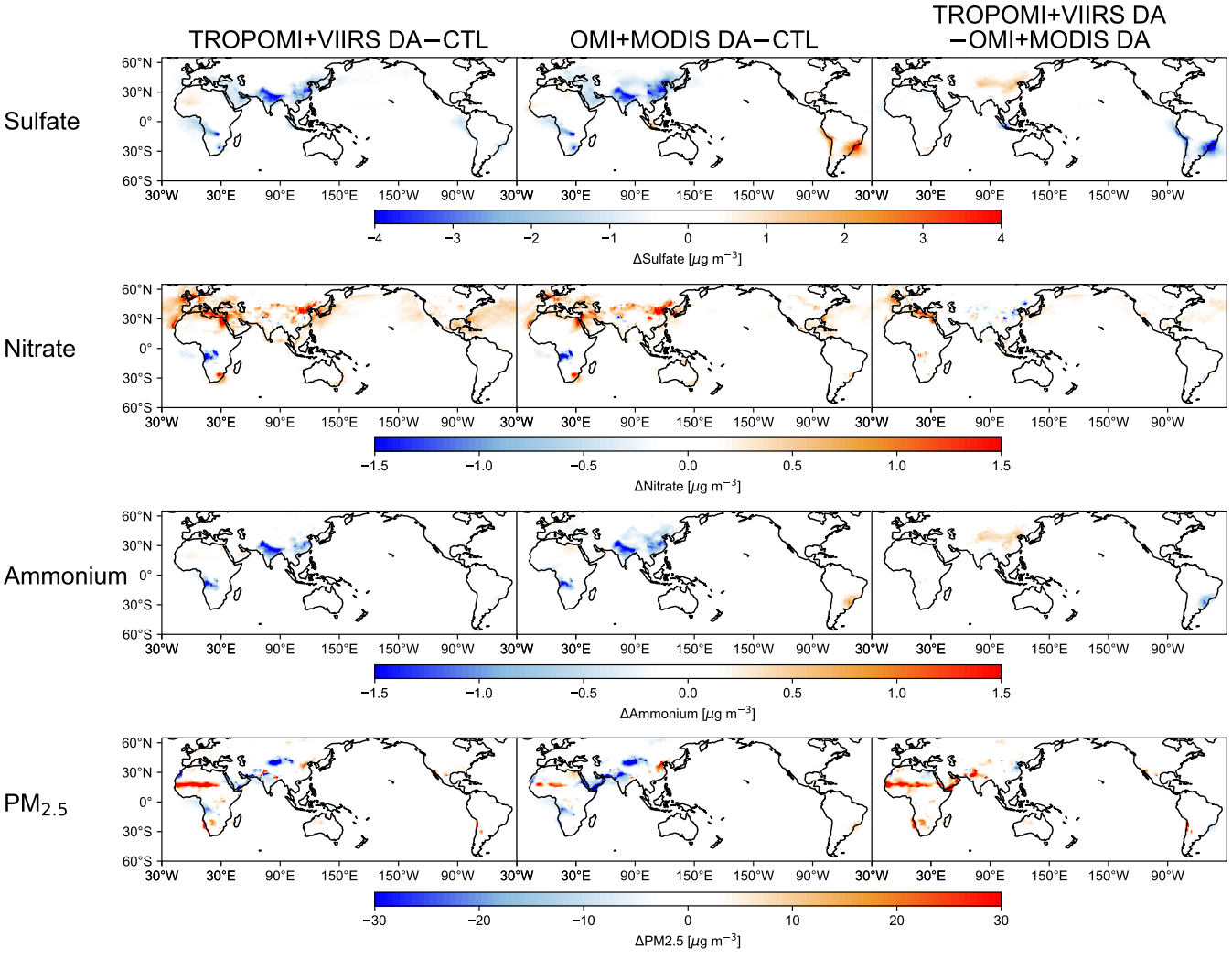

Figure 10. Surface sulfate (first row), nitrate (second row), ammonium (third row), and fine particulate matters ($PM_{2.5}$; fourth row) concentration changes due to TROPOMI+VIIRS DA (left) and OMI+MODIS DA (center), compared to the control simulation, during June–August 2018. The right column shows the difference between the TROPOMI+VIIRS and OMI+MODIS DA runs. The unit is μg m^{-3}.

Table 1. List of assimilated satellite observations

Satellite/Intrument	Variable	Product version	Screening criteria	Reference
Aura/OMI	NO_2 tropospheric column	QA4ECV v1.1	CRF < 0.5 SZA $< 81°$ SA < 0.3 QF $= 0$ tropAMF/geoAMF > 0.1	Boersma et al. (2017, 2018)
Aura/OMI	SO_2 column	OMSO2 V2	CRF < 0.2 SZA $< 70°$ CTP $>$ first 10 and CTP $<$ last 10	Li et al. (2013, 2020a, b)
Aura/MLS	Ozone and HNO_3 profiles	V4.2	p <215 hPa (for ozone) p <150 hPa (for HNO_3) SF=odd QF<1 Conv.>1.03	Livesey et al. (2011) Schwartz et al. (2015) Manney et al. (2015)
Terra/MOPITT	CO total column	V7 TIR-NIR product	|Lat| <65° Daytime data	Deeter et al. (2017)
Aqua and Terra/MODIS	Aerosol Optical Depth (AOD)	Collection 6.1	see Section 2.1.3	Sayer et al. (2013)
S5P/TROPOMI	NO_2 tropospheric column	v2.4-	QA value>0.75	van Geffen et al. (2022)
S5P/TROPOMI	SO_2 column	COBRA v2	recalculated QA value>0.5	Theys et al. (2021)
S-NPP and NOAA20/VIIRS	Aerosol Optical Depth (AOD)	v2	see Section 2.1.3	Lee et al. (2024)

CRF: cloud radiance fraction, SZA: solar zenith angle, QF: quality flag, tropAMF: tropospheric AMF, geoAMF: geometric AMF, CTP: cross-track pixels, p: pressure, SF: status flag

https://doi.org/10.5194/egusphere-2026-1681
Preprint. Discussion started: 27 April 2026

Table 2. List of data assimilation calculations performed in this study.

ID	Period	Assimilated observations	
		Trace gases (NO_2 and SO_2)	AOD
GasAero	April–August 2016	OMI	MODIS
Gas-only		OMI	
Aero-only			MODIS
OMI+MODIS	May–August 2018	OMI	MODIS
TROPOMI+VIIRS		TROPOMI	VIIRS
CTL	April–August 2016 May–August 2018		

https://doi.org/10.5194/egusphere-2026-1681
Preprint. Discussion started: 27 April 2026

Table 3. Statistical scores of validation using independent observations for GasAero DA, Aero-only DA, Gas-only DA, and CTL during May–August 2016. MB, S-Corr, and RMSE indicate mean bias, spatial correlation coefficient, and root mean square error, respectively. The boldface values denote the best performance among the data assimilation and the control simulation. The MB and RMSE of aerosol mass concentrations are μg m^{-3}.

Observation data	GasAero DA			Aero-only DA			Gas-only DA			CTL		
	MB	S-Corr	RMSE	MB	S-Corr	RMSE	MB	S-Corr	RMSE	MB	S-Corr	RMSE
AERONET AOD	-0.04	**0.90**	**0.07**	-0.03	**0.90**	**0.07**	-0.06	0.67	0.13	**0.01**	0.78	0.11
KORUS-AQ Sulfate (>750 hPa)	**0.06**		**3.20**	2.81		4.97	-1.29		3.41	1.57		4.41
KORUS-AQ Nitrate (>750 hPa)	0.74		4.91	-0.77		4.28	**0.03**		4.64	-1.24		**4.05**
KORUS-AQ Ammonium (>750 hPa)	**0.07**		2.31	0.55		2.39	-0.58		2.41	-0.24		**2.15**
CASTNET Sulfate	**-0.03**	**0.65**	**0.40**	0.30	**0.65**	0.58	-0.13	0.64	**0.40**	0.20	0.59	0.58
CASTNET Nitrate	0.05	0.44	**0.25**	-0.22	**0.51**	0.29	**0.03**	0.43	**0.25**	-0.14	0.37	0.26
CASTNET Ammonium	**0.005**	0.73	**0.12**	0.02	**0.74**	0.13	-0.02	0.71	**0.12**	0.03	0.73	0.15
AQS $PM_{2.5}$	**-0.46**	**0.80**	**1.28**	-0.50	0.78	1.33	-0.84	**0.80**	1.43	-1.75	0.46	2.55
EMEP Sulfate	0.87	0.13	0.96	1.17	**0.40**	1.28	**0.76**	0.06	**0.87**	1.09	0.37	1.20
EMEP Nitrate	0.22	0.21	0.49	**-0.01**	0.22	**0.30**	0.20	0.22	0.45	0.02	0.22	0.32
EMEP Ammonium	-0.014	**0.41**	**0.26**	0.017	**0.41**	0.28	-0.05	0.40	**0.26**	**0.010**	0.40	0.29
AQ e-rep. $PM_{2.5}$	-1.51	0.13	**12.4**	**-1.46**	0.14	12.5	-1.51	0.13	**12.4**	-1.71	**0.15**	12.5
EANET Sulfate	**-0.14**	0.77	**0.86**	0.64	0.82	1.26	-0.38	0.75	0.93	0.63	**0.83**	1.21
EANET Nitrate	**-0.15**	0.36	**0.50**	-0.39	0.31	0.57	-0.16	0.36	**0.50**	-0.37	**0.39**	0.55
EANET Ammonium	**-0.002**	0.61	0.36	0.07	**0.66**	**0.35**	-0.07	0.53	0.39	0.05	0.58	0.38
Japan/AirKorea $PM_{2.5}$	**1.13**	**0.82**	**4.52**	2.50	0.81	5.27	-4.32	0.76	5.86	-1.42	0.70	4.53

https://doi.org/10.5194/egusphere-2026-1681
Preprint. Discussion started: 27 April 2026

Table 4. Global and regional total emissions of carbonaceous (Carb), dust, SO_2, and NO_x. The *a posteriori* emissions are derived from the GasAero, Gas-only, and Aero-only DAs (first to third column), while the *a priori* emissions (fourth column) are taken from the bottom-up emission inventories (CEDS v2021_04_21 and GFED4.1s) and online calculation in the forecast model. The unit is Tg/yr. Region definition is shown in Fig. S5.

Region	GasAero DA				Aero-only DA				Gas-only DA				*A priori*			
	Carb	Dust	SO_2	NO_x	Carb	Dust	SO_2	NO_x	Carb	Dust	SO_2	NO_x	Carb	Dust	SO_2	NO_x
Global	103.3	1257.9	29.6	63.6	99.0	1194.8	43.8	41.1	85.3	3046.2	29.6	63.4	85.3	3046.2	43.8	41.1
China	17.7	17.5	3.4	10.2	16.4	22.6	8.4	7.0	5.8	72.0	3.4	10.2	5.8	72.0	8.4	7.0
USA	2.5	8.2	1.5	6.3	2.7	8.4	2.2	3.5	1.6	32.1	1.5	6.2	1.6	32.1	2.2	3.5
Europe	2.4	16.9	1.3	5.2	2.2	18.5	2.5	3.2	1.6	31.4	1.3	5.1	1.6	31.4	2.5	3.2
SE. Asia	6.1	0.0	0.5	1.7	6.0	0.0	1.0	1.1	2.3	2.1	0.5	1.7	2.3	2.1	1.0	1.1
India	5.0	219.3	2.0	4.0	3.4	208.2	5.2	2.8	6.4	449.0	2.0	3.9	6.4	449.0	5.2	2.8
N. Africa	3.7	518.8	0.7	3.3	3.6	457.8	1.2	2.0	3.9	878.6	0.7	3.4	3.9	878.6	1.2	2.0
C. Africa	23.6	8.5	0.8	4.3	22.1	9.3	1.3	5.1	21.3	45.9	0.8	4.3	21.3	45.9	1.3	5.1
S. Africa	0.1	0.0	0.7	0.4	0.1	0.0	1.2	0.3	0.2	0.3	0.7	0.4	0.2	0.3	1.2	0.3
S. America	4.4	0.0	0.5	1.2	4.3	0.1	0.3	1.3	6.4	4.3	0.5	1.2	6.4	4.3	0.3	1.3
Middle East	0.3	142.8	1.0	1.2	0.3	127.4	2.6	0.8	0.2	476.5	1.0	1.2	0.2	476.5	2.6	0.8

https://doi.org/10.5194/egusphere-2026-1681
Preprint. Discussion started: 27 April 2026

Table 5. Statistical scores of validation using independent observations for TROPOMI+VIIRS DA, OMI+MODIS DA, and CTL during June–August 2018. MB, S-Corr, and RMSE indicate mean bias, spatial correlation coefficient, and root mean square error, respectively. The boldface values denote the best performance among the data assimilation and the control simulation. The MB and RMSE of aerosol mass concentrations are μg m^{-3}.

Observation data	TROPOMI+VIIRS DA			OMI+MODIS DA			CTL		
	MB	S-Corr	RMSE	MB	S-Corr	RMSE	MB	S-Corr	RMSE
AERONET	**-0.003**	**0.83**	**0.061**	-0.016	0.66	0.086	-0.043	0.66	0.100
ATom-4 Sulfate (>750 hPa)	**0.23**		**0.76**	0.28		0.88	0.25		0.84
ATom-4 Nitrate (>750 hPa)	-0.007		0.07	0.01		**0.05**	**0.005**		0.08
ATom-4 Ammonium (>750 hPa)	0.005		0.16	**0.002**		0.15	-0.01		**0.13**
CASTNET Sulfate	**0.11**	0.57	**0.52**	0.13	**0.59**	**0.52**	0.19	0.49	0.64
CASTNET Nitrate	-0.06	0.29	**0.35**	**-0.05**	0.32	**0.35**	-0.19	**0.44**	0.36
CASTNET Ammonium	0.02	0.59	**0.14**	0.02	**0.64**	**0.14**	**0.005**	0.60	0.15
AQS $PM_{2.5}$	**-0.99**	0.42	**2.23**	-1.00	0.35	2.42	-1.75	**0.46**	2.55
EMEP Sulfate	**0.53**	-0.01	**0.72**	0.72	-0.30	0.93	0.73	**0.04**	0.92
EMEP Nitrate	-0.08	0.03	**0.56**	**-0.06**	**-0.13**	0.58	-0.25	0.004	**0.56**
EMEP Ammonium	-0.15	0.47	0.28	**-0.12**	0.46	**0.26**	-0.13	**0.49**	0.27
AQ e-rep. $PM_{2.5}$	-1.51	**0.18**	**7.43**	**-1.10**	0.10	7.45	-2.26	0.09	7.72
EANET Sulfate	**-0.19**	**0.73**	0.92	-0.21	**0.73**	**0.90**	0.24	0.72	0.94
EANET Nitrate	**-0.23**	**0.63**	**0.42**	-0.28	**0.63**	0.46	-0.42	0.59	0.58
EANET Ammonium	-0.05	0.25	0.35	-0.05	**0.32**	**0.34**	**-0.007**	**0.32**	**0.34**
Japan/AirKorea $PM_{2.5}$	-0.61	0.66	4.56	**-0.01**	**0.68**	**4.05**	-2.18	0.65	4.19